International Journal of Mining Science and Technology 35 (2025) 1809–1826

Contents lists available at ScienceDirect

International Journal of Mining Science and Technology

journal homepage: www.elsevier.com/locate/ijmst

Failure characteristics and mechanisms of uniaxial compressed red sandstone in non-uniform water distribution environment: Effects of immersion height and duration

Jiancheng Huang [a], Yong Luo [a,*], Xuefeng Si [a], Feng Lin [b], Kun Wang [c], Jiadong Qiu [a], Fan Feng [d], Qing Du [a]

[a] School of Resources Environment and Safety Engineering, University of South China, Hengyang 421001, China
[b] Key Laboratory of Ministry of Education on Safe Mining of Deep Metal Mines, Northeastern University, Shenyang 110819, China
[c] China Coal Technology and Engineering Group Shenyang Research Institute Co., Ltd., Fushun 113122, China
[d] College of Energy and Mining Engineering, Shandong University of Science and Technology, Qingdao 266590, China

ARTICLE INFO

Article history:
Received 27 May 2025
Received in revised form 22 August 2025
Accepted 18 September 2025
Available online 4 November 2025

Keywords:
Immersion height
Immersion duration
Non-uniform water distribution
Strength weakening
Failure mechanism
Red sandstone

ABSTRACT

To investigate the influence of non-uniform water distribution on the mechanical properties and failure behavior of red sandstone, we designed five immersion heights and durations to achieve varying non-uniform water distribution states. Uniaxial compression tests were conducted on red sandstone under these conditions. The effects of non-uniform water distribution on deformation, failure, strength, and energy characteristics of red sandstone were analyzed. The impact of non-uniform water distribution on the intensity of rock failure was discussed, and the failure mechanism under non-uniform water distribution was revealed. The hazards of low immersion heights on underground rock structures were analyzed. The results demonstrate that peak strength and elastic modulus of red sandstone exhibit high sensitivity to immersion height, with reductions of 38% and 23% respectively even at $L=1/50H$. Water immersion reduces both energy storage capacity and energy dissipation capability of red sandstone. The immersion height and duration influence the failure mode of red sandstone by controlling the migration and separation of dry-wet interfaces. Low immersion height poses significant risks to underground rock structures (e.g., a 38% strength reduction when $L=1/50H$), and the concentration degree of water non-uniform distribution is the key factor in assessing the weakening effect of water on rocks.

1. Introduction

Water is not only one of the key factors affecting rock properties, but also the most commonly encountered geological fluid in underground rock engineering. Under the influence of groundwater activity, the mechanical properties of rocks undergo significant changes, severely affecting the stability of underground rock structures such as mine pillars and tunnel surrounding rocks [1,2]. In 1960, Price [3] reported that the uniaxial compressive strength (σ_c) of rocks decreases with increasing water content. Subsequent extensive research has investigated the effects of water on the uniaxial compressive (UC) mechanical properties of sedimentary rocks [4], igneous rocks [5], metamorphic rocks [6], and rock-like materials [7]. These studies demonstrate that the σ_c and elastic modulus (E_0) of rocks predominantly exhibit either exponential or linear relationships with water content. Wong et al. [8] reviewed studies on the impact of water on the UC mechanical properties of rocks before 2015 and statistically analyzed the percentage loss of σ_c across various rock types (see Fig. 1). The results indicate that 81.38% of rocks exhibit a σ_c loss of less than 60%, while 18.62% demonstrate a loss exceeding 60%. Currently, research on the impact of water on rocks from an energetic perspective is receiving increasing attention. Studies have shown that water can significantly reduce the peak elastic energy and peak dissipated energy of rocks [9]. For example, Khan et al. [10] predicted the early failure points of sandstone with different water contents by analyzing the evolution of the ratios of elastic energy density to dissipated energy density. Zhou et al. [11] pointed out that water inhibits the rockburst tendency of sandstone by reducing its pre-peak elastic energy and post-peak energy release rate. Luo et al. [12] found that water has no significant effect on the ratio of peak elastic energy to peak input energy in sandstone. Furthermore, water significantly affects the failure characteristics of rocks. For example, Li et al. [13] reported that dry specimens exhibited X-shaped conjugate shear failure, natural-state specimens showed mixed

---

[*] Corresponding author.
E-mail address: luoyong@usc.edu.cn (Y. Luo)

https://doi.org/10.1016/j.ijmst.2025.09.008

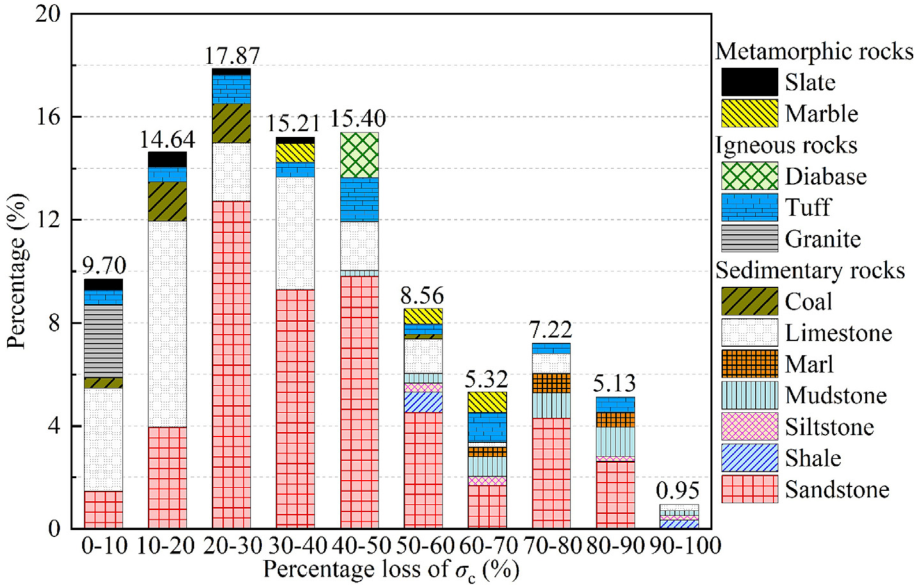

Fig. 1. Distribution of percentage loss of σ_c (modified from Cai et al. [16]).

X-shaped conjugate shear and tensile failure, while saturated specimens demonstrate tensile failure accompanied by X-shaped shear cracks. Zhou et al. [14] found that the crack propagation speed in sandstone specimens significantly decreased with increasing water content. Cai et al. [15] noted that dry sandstone primarily fails through intragranular fracture of quartz particles, whereas saturated sandstone exhibits intergranular fracture. The above studies have clarified the effects of water on rock energy and failure, but they primarily focused on rocks under complete immersion conditions (i.e., uniform water distribution).

However, in underground rock engineering, due to varying degrees of water seepage, water inrush, and water usage, the rock is often subjected to different immersion heights (L) rather than being in a full immersion state, leading to non-uniform water distribution within the rock. For example, mine pillars or surrounding rocks of tunnels may have only localized regions affected by water immersion, while the rest remain exposed to air, ultimately resulting in a non-uniform water distribution within the mine pillars or surrounding rock [1,17]. Existing studies indicate that water distribution cause by different L significantly affects rock mechanical properties. For instance, Chen et al. [1] and Yu et al. [18] revealed that the σ_c of partially immersed rocks decreases linearly in two stages with increasing water content, whereas fully immersed rocks follow an exponential decline. Luo et al. [19] demonstrated that UC red sandstone specimens with different L exhibited pronounced asymmetric failure characteristics, with fractures predominantly concentrated in the water immersion section. Liu et al. [17] revealed that the duration of compression and yielding stages increased significantly with greater L, while the elastic stage duration remained relatively unchanged. Liu et al. [20] established a damage constitutive model for soft sandstone based on damage variables of σ_c and E_0 under different L. However, these studies primarily focused on non-uniform water distribution within rocks induced by L. In fact, in addition to L, immersion duration (t) is another critical factor affecting water distribution in rocks. In actual engineering projects, under different conditions, the underground surrounding rock may be subjected to water immersion with varying durations. For example, water diversion tunnels and residual pillars in goaf areas may be subjected to long-term water immersion, while tunnels under construction or in operation and pillars in active mining areas may only experience short-term water immersion due to timely drainage. Under the same L, different t lead to significant differences in water distribution within rocks, i.e., the water distribution within rocks is affected not only by the L but also by the t. Therefore, simultaneously considering both L and t to investigate the effects of non-uniform water distribution on rock mechanical properties and failure behavior under varying L and t is of great significance.

In this study, taking L and t as control factors, designing an orthogonal experiment incorporating five different L and five different t to achieve the varying non-uniform water distribution states. A series of UC tests were conducted on red sandstone with non-uniform water distribution. The influence of non-uniform water distribution on the mechanical behavior of red sandstone was analyzed from three aspects: mechanical properties, energy characteristics, and failure patterns. The relationship between the failure intensity and non-uniform water distribution of red sandstone was discussed. The failure mechanisms of red sandstone under different non-uniform water distributions were investigated. The potential hazards of low L on underground rock structures were assessed. The findings of this study contribute to understanding the failure mechanism of non-uniform water distribution in underground rocks caused by incomplete immersion, and provide theoretical support for the stability assessment of these underground rocks.

2. Experimental materials and methods

2.1. Experimental material

In this study, red sandstone from the Shandong Province of China was selected as the research subject. X-ray diffraction analysis revealed that the mineral composition of the red sandstone primarily consists of quartz (53.4%), albite (25.7%), calcite (18.3%), along with minor amounts of chlorite (1.1%), montmorillonite (0.8%), and laumontite (0.7%) (see Fig. 2a). The red sandstone contains no apparent bedding planes or fractures (see Fig. 2b). The mean density and longitudinal wave velocity of the red sandstone under natural conditions are 2.53 g/cm^{3}and 4.176 km/s, respectively. The coefficients of variation are 0.57% for density and 4.49% for longitudinal wave velocity. Microstructural analysis indicated that the particle boundaries of the red sandstone are distinct

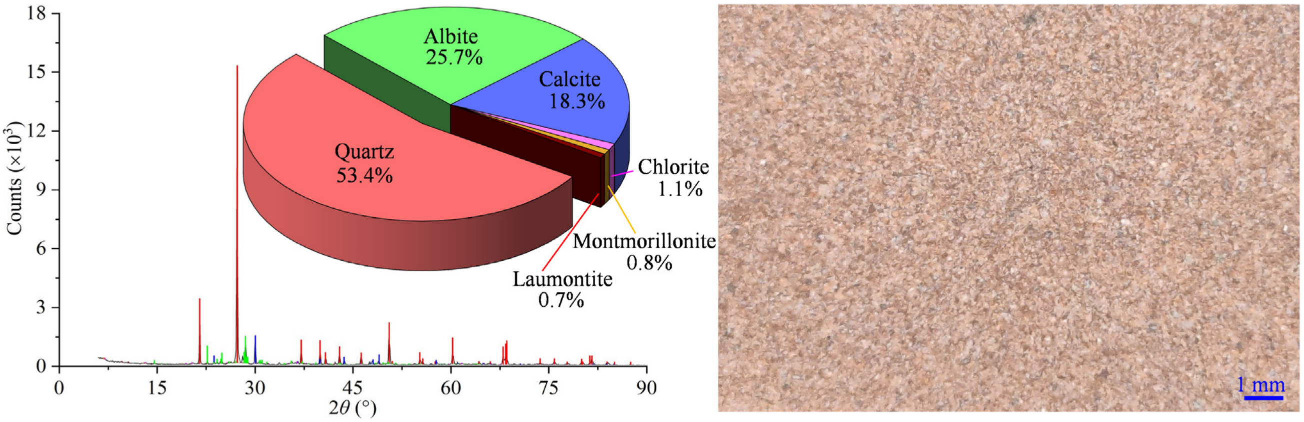

(a) Mineral composition (b) Macroscopic observation

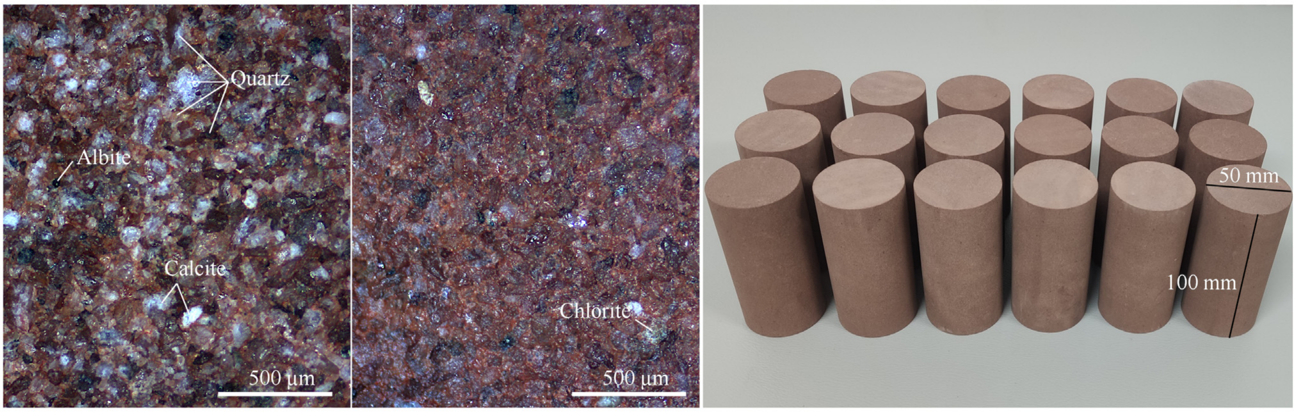

(c) Observation in dry (d) Observation in saturated (e) Standard cylindrical specimens

Fig. 2. Red sandstone materials.

under dry conditions, but become blurred in the saturated state due to water absorption and swelling of clay minerals (chlorite and montmorillonite) (see Figs. 2c and d). The processed cylindrical red sandstone specimens (Φ50 mm × 100 mm) are shown in Fig. 2e. All specimens were cored from the same rock block with consistent orientation. During specimen selection, only those with defect-free surfaces, similar longitudinal wave velocities, and end faces meeting the parallelism and perpendicularity requirements recommended by the ISRM were retained to reduce experimental errors [21].

2.2. Experimental methods

First, natural-state specimens were placed in a constant temperature drying oven at 110±0.5 ℃ for 24 h to obtain dried specimens. They were then wrapped with waterproof film to prevent water absorption [1], as shown in Fig. 3a. Subsequently, the dried specimens were immersed in deionized water at room temperature and atmospheric pressure according to predetermined L. They were periodically removed, surface-dried, and weighed to measure the dynamic changes in water absorption rate (W_t, Fig. 3b). Five L (L=1/50H, 1/8H, 1/4H, 1/2H, and H, where H represents the specimen height) and five t (t=1, 5, 20, 40, and 211 h) were set to simulate different immersion conditions in underground surrounding rocks. The 211 h is the maximum time required for the W_t of all L specimens to reach stability. The specific experimental scheme is presented in Table 1. During testing, dried specimens were treated following the schemes in Table 1. Upon reaching the designated t, the specimens were immediately retrieved, weighed to calculate the W_t, and subsequently tested mechanically (see Fig. 3c). The tests were conducted on an RMT-150B rock mechanics testing system under UC at a constant loading rate of 0.2 kN/s. The entire failure process of the specimens was recorded using high-resolution photography.

3. Water absorption properties of red sandstone

Fig. 4a shows the variation curves of W_t of specimens under different L with t. The water absorption processes under all L exhibit significant three stage characteristics, i.e., the rapid growth stage, transitional slowing stage, and stable stage. During the rapid absorption stage, all specimens demonstrate a nonlinear rapid increase in W_t with increasing t, but the growth rate gradually slows. The L exerts a significant influence on the W_t, which is characterized by a progressive increase in the W_t as the L rises. Additionally, the transition time from the rapid growth stage to the transitional slowing stage is similar across different L (approximately 91 h). In the transitional slowing stage, the W_t growth slows considerably, indicating a gradual slowdown in internal water absorption. In the stable stage, the time required to reach water absorption equilibrium increases with higher L, but this time becomes consistent when $L \geq 1/4H$. At 211 h, all specimens reach a stable state of water absorption. Fig. 4b illustrates the relationship between W_t and L at different t. Under the same t, the W_t increases with higher L, and this increase can be divided into two distinct

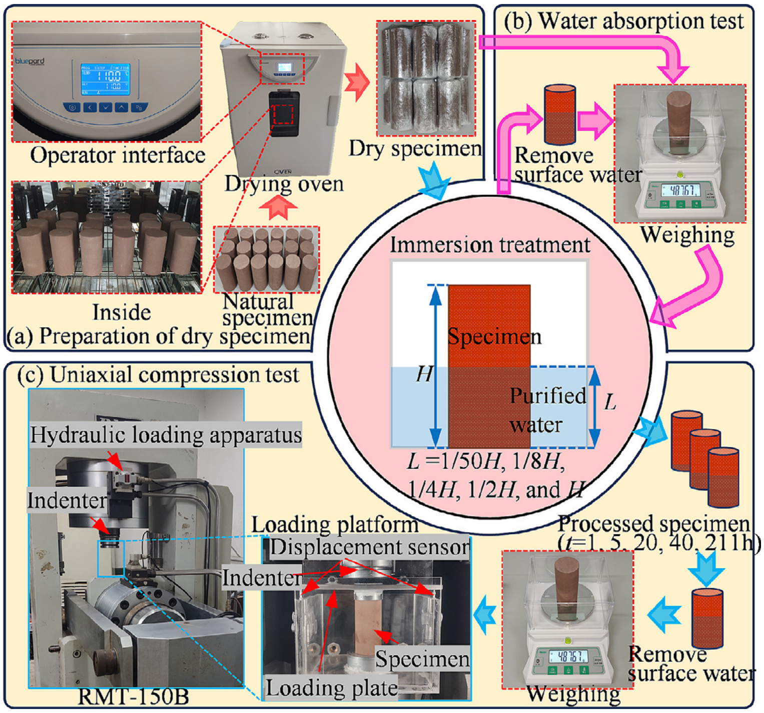

Fig. 3. Schematic diagram of the experimental procedure.

Table 1
Experimental scheme.

L	*t*				
	1 (h)	5 (h)	20 (h)	40 (h)	211 (h)
1/50*H*	S1/50–1	S1/50–5	S1/50–20	S1/50–40	S1/50–211
1/8*H*	S1/8–1	S1/8–5	S1/8–20	S1/8–40	S1/8–211
1/4*H*	S1/4–1	S1/4–5	S1/4–20	S1/4–40	S1/4–211
1/2*H*	S1/2–1	S1/2–5	S1/2–20	S1/2–40	S1/2–211
H	S1-1	S1-5	S1-20	S1-40	S1-211

phases: a sharp rise when $L<1/50H$ and a slower linear increase when $L\geq1/50H$. At $L=1/50H$, the W_t at 1, 5, 20, 40, and 211 h reaches 26.1%, 27.3%, 44.4%, 49.8%, and 48.3% of the corresponding values at $L=H$, respectively. At $L=1/2H$, the W_t at these times reaches 71.3%, 71.9%, 70.4%, 77.8%, and 81.3% of the values at $L=H$, respectively.

Fig. 5 illustrates the non-uniform water distribution on the surface of red sandstone specimens under different *L*. Observations reveal that a moistened zone appears in a broad area above the *L* in partially immersed specimens, demonstrating significant capillary effects in red sandstone. However, the upper boundary of the moistened zone is not horizontal, but exhibits an irregular wave shape. The height of the moistened zone generally increases with rising *L* and extended *t*. This irregular, wave-like top boundary of the moistened zone may result from differences in the spatial distribution of internal pore structure, hydrophilic and hydrophobic minerals in the specimen.

These results indicate that *L* and *t* significantly affect the W_t and distribution in red sandstone. Even at very low *L*, the W_t can reach nearly half of that under full immersion conditions when given sufficient *t*. In addition, the water distribution of red sandstone is also influenced by its internal pore structure, hydrophilic and hydrophobic minerals.

4. Mechanical testing results and analysis

4.1. Strength and deformation characteristics

The stress–strain curves of red sandstone specimens under different water immersion conditions exhibit four distinct stages: compaction stage, elastic stage, yield stage, and post-peak stage (see Fig. 6). These stages correspond to the internal pore and fracture compaction, elastic deformation, unstable crack propagation, and loss of bearing capacity, respectively [22]. Under the same *L*, with increasing *t*, the slope of the elastic stage, peak strain, and area enclosed by the stress–strain curve all demonstrate a decreasing trend. Moreover, under longer *t* and higher *L*, specimens exhibit more pronounced pre-peak yield behavior and a slower post-peak stress drop. For example, specimens with $L\geq1/2H$ exhibit a noticeable slowdown in curve slope approaching the peak, while dry, S1/50–1, S1/50–5, S1/8–1, S1/8–5, and S1/4–1 specimens display abrupt post-peak stress drops. The differences in mechanical behavior are primarily attributed to the softening effect of water on red sandstone. Increased *L* expands the softening range of red sandstone, and prolonged *t* enhances the softening degree. Therefore, the coupling effect of greater *L* and longer *t* leads to more significant softening in red sandstone specimen, manifested as more

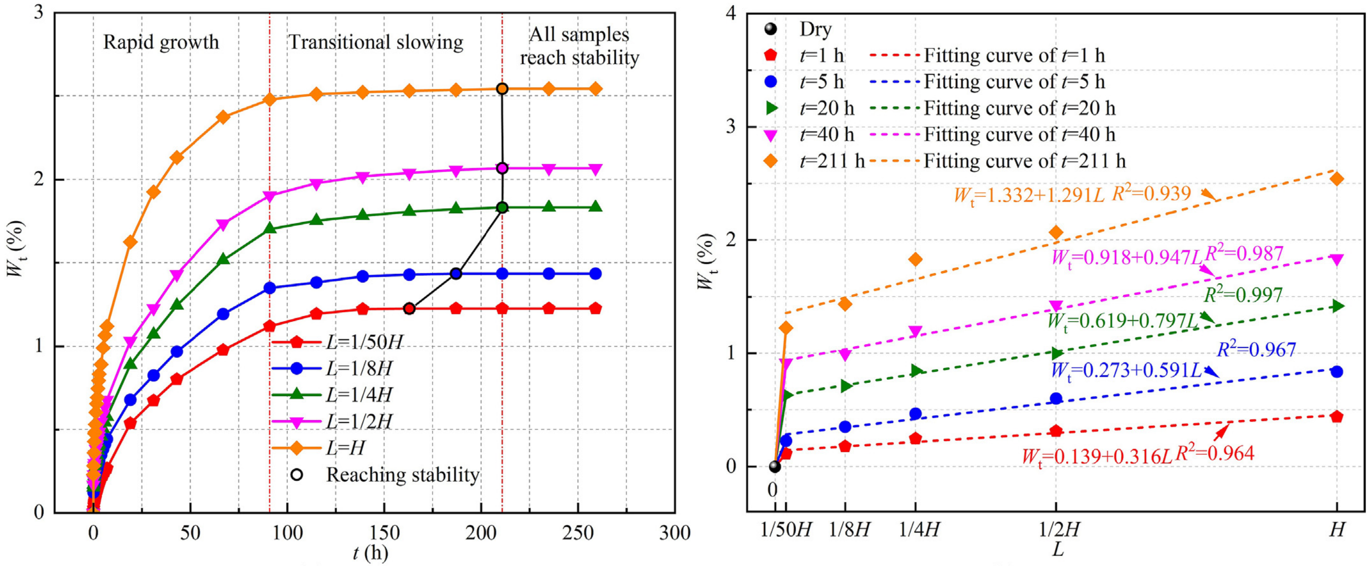

(a) W_t versus t (b) W_t versus L

Fig. 4. Water absorption behavior of red sandstone.

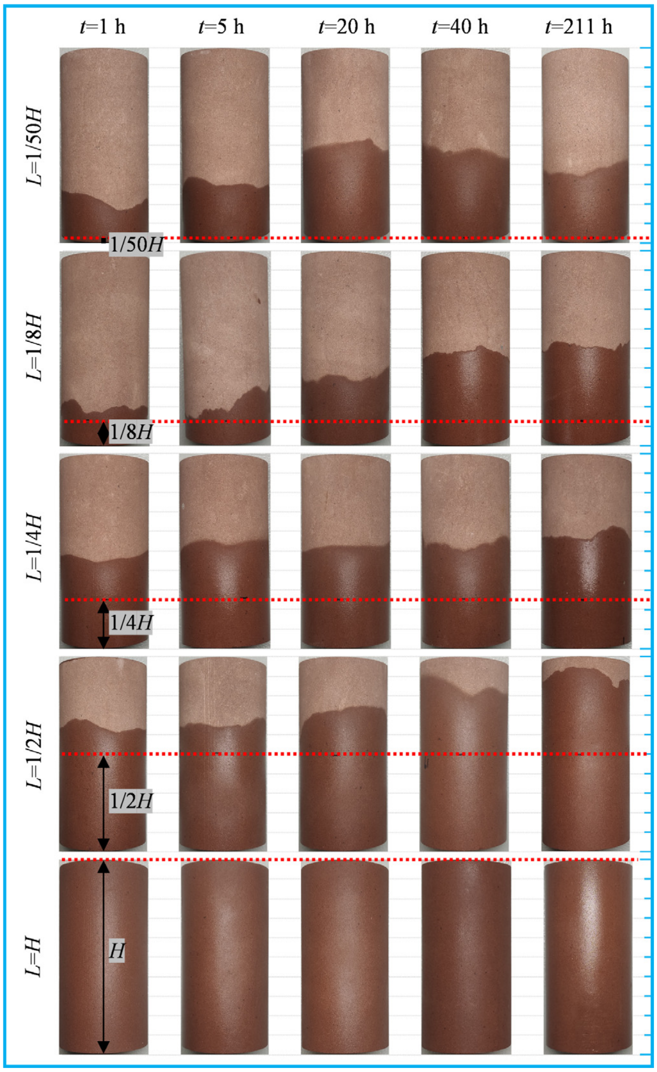

Fig. 5. Non-uniform water distribution on specimen surface under different immersion conditions.

prominent pre-peak yield stage and slower post-peak stress reduction.

The non-uniform water distribution caused by t and L is a critical factor affecting the σ_c of red sandstone (see Fig. 7). The σ_c of specimens under all L exponentially decreases with increasing t (Fig. 7a). Specifically, the σ_c of the dry specimen is 160.9 MPa. At t=20 h, the σ_c for L=1/50H, 1/8H, 1/4H, 1/2H, and H decreased to 115.5 (28.2% reduction), 112.0 (30.4% reduction), 111.5 (30.7% reduction), 110.9 (31.1% reduction), and 102.4 MPa (36.4% reduction), respectively. At t=211 h, the corresponding values further dropped to 99.7 (38.0% reduction), 95.8 (40.5% reduction), 94.8 (41.1% reduction), 88.4 (45.1% reduction), and 81.2 MPa (49.5% reduction). This indicates that the major reduction in σ_c for all L occurred within the first 20 h during immersion. Simultaneously, the variation in σ_c with L under all immersion conditions exhibited a distinct two-stage pattern: a sharp strength decline when $L \leq 1/50H$, followed by a slower linear reduction when $L > 1/50H$ (see Fig. 7b). At L=1/50H, the σ_c at t=1, 5, 20, 40, and 211 h decreased to 147.3 (8.5% reduction), 137.4 (14.6% reduction), 115.5 (28.2% reduction), 107.8 (33.0% reduction), and 99.7 MPa (38.0% reduction), respectively. At L=H, the corresponding values were 136.6 (15.1% reduction), 114.9 (28.6% reduction), 102.4 (36.4% reduction), 97.0 (39.7% reduction), and 81.2 MPa (49.5% reduction). These results highlight the extreme sensitivity of red sandstone strength to L, with significant weakening occurring even under extremely low L (L=1/50H).

Fig. 8 illustrates the variation of E_0 with t and L. Under different L, the E_0 exhibits an exponential decline with increasing t (Fig. 8a). Meanwhile, under varying t, the relationship between E_0 and L shows distinct two-stage characteristics: a sharp decrease when $L \leq 1/50H$, followed by a gradual linear downward trend when $L > 1/50H$ (Fig. 8b). This indicates that the E_0 follows a reduction pattern, which is similar to that of the σ_c.

4.2. Energy characteristics

The energy characteristics comprehensively reflect the strength and deformation properties of rock materials and are closely related to failure behavior [23,24]. Therefore, the influence of non-uniform water distribution caused by different L and t on

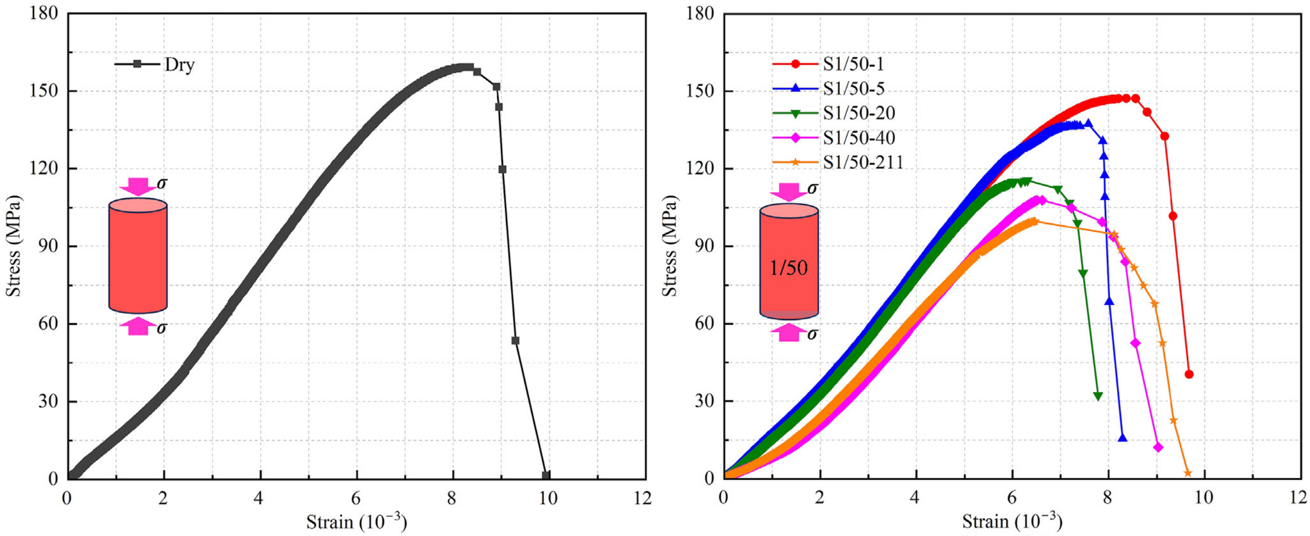

(a) Dry state

(b) *L*=1/50*H*

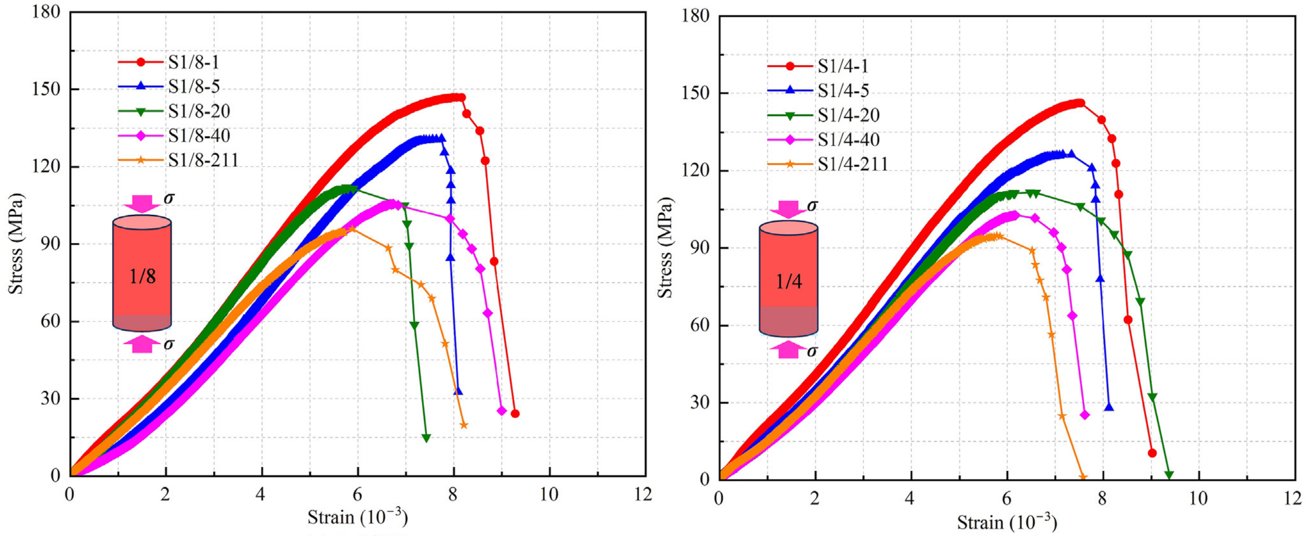

(c) *L*=1/8*H*

(d) *L*=1/4*H*

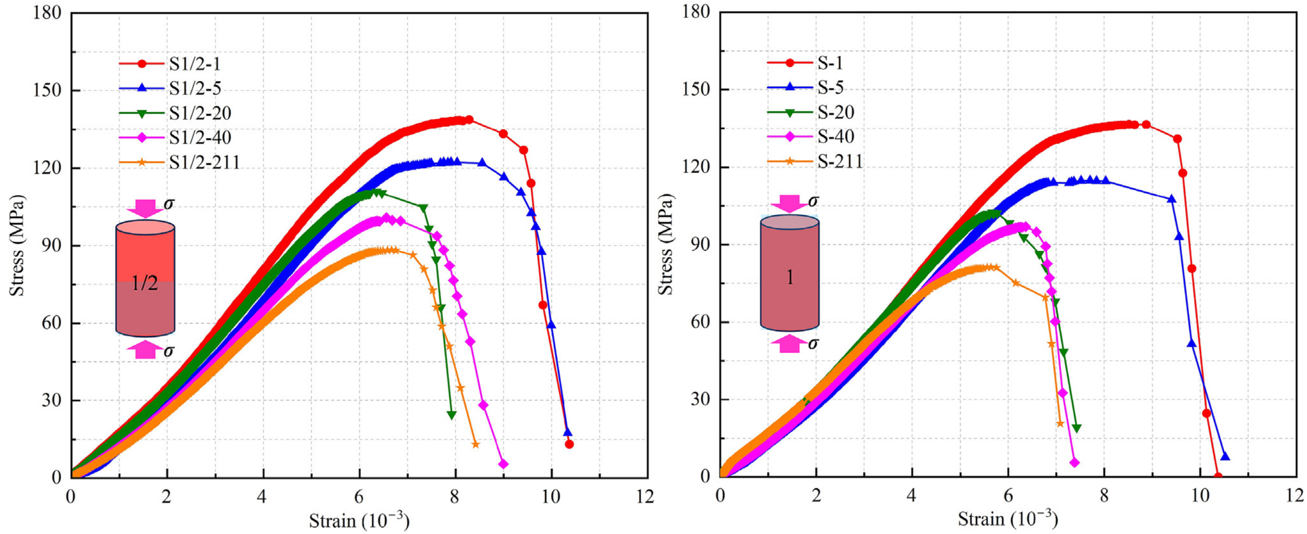

(e) *L*=1/2*H*

(f) *L*=*H*

Fig. 6. Stress–strain curves under different immersion conditions.

red sandstone is analyzed from an energy perspective. Based on the first law of thermodynamics, assuming that rock energy exists solely in the form of elastic energy and dissipated energy, the energy balance equation can be established, as shown in Eq. (1). The input energy density (u_t) can be obtained by integrating the stress–strain curve [25]. Heap et al. [26] and Li and Cai [27] demon-

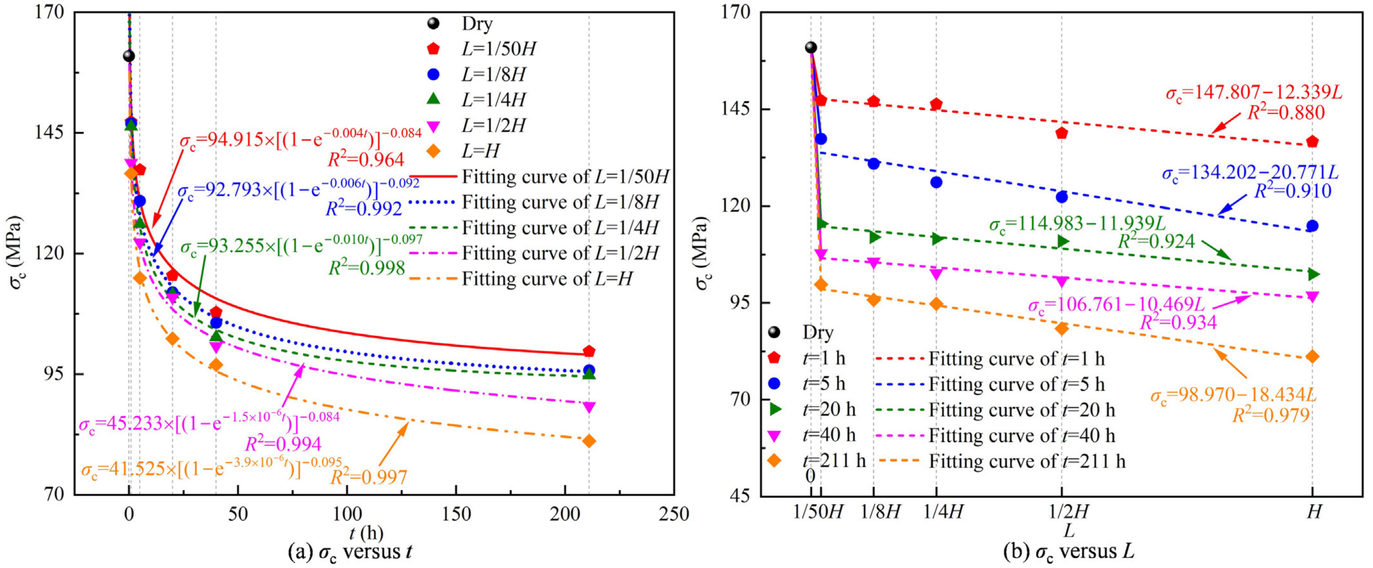

(a) σ_c versus t (b) σ_c versus L

Fig. 7. Effects of t and L on σ_c.

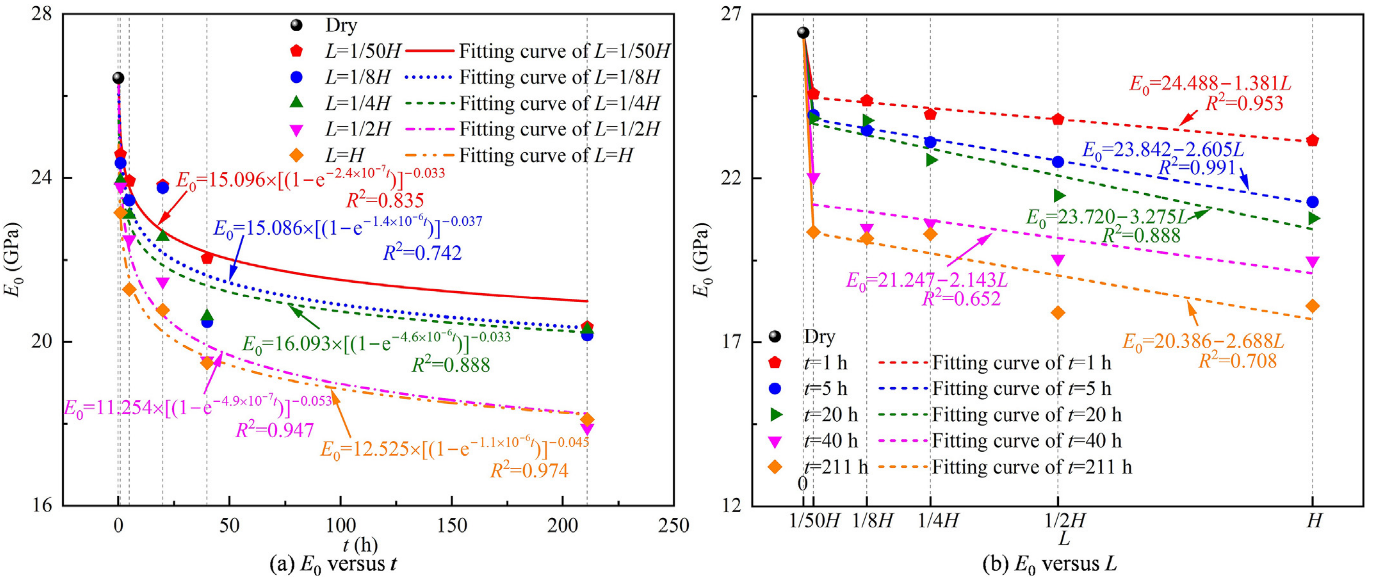

(a) E_0 versus t (b) E_0 versus L

Fig. 8. Effects of t and L on E_0.

strated that the elastic energy density (u_e) can be calculated using the E_0 and stress (σ) through Eq. (2). Following this theory, energy parameters such as u_t, u_e, and dissipated energy density (u_d) of red sandstone specimens can be obtained. The evolution of u_d reflects the damage state of the specimens. Thus, the energy dissipation rate (G_d) is introduced to further analyze the energy dissipation behavior of the specimens [28,29], as shown in Eq. (3).

$$u_t + u_e = u_d \tag{1}$$

$$u_e = \frac{\sigma^2}{2E_0} \tag{2}$$

$$G_d = \frac{du_d}{dt} \tag{3}$$

Fig. 9 illustrates the energy evolution process of red sandstone under various water immersion conditions during UC (taking dry, S1/2–1, S1/2–5, S1/2–20, S1/2–40, and S1/2–211 specimens as examples, with similar patterns observed for other conditions). The energy evolution process can be divided into four distinct stages:

Stage I: The u_e exhibits an accelerating growth trend, while the u_d increases at an extremely low rate to a minimal value, with the G_d approaching zero. In this stage, the compaction effect of internal pores and fractures leads to energy dissipation, resulting in a relatively low initial growth rate of u_e. As the compaction process progresses, the energy consumed for compaction gradually decreases, causing the growth rate of u_e to accelerate.

Stage II: The u_e grows approximately linearly, and the u_d does not increase significantly. The u_e curve remains nearly parallel to the u_t curve, with the G_d remaining close to zero. This phenomenon

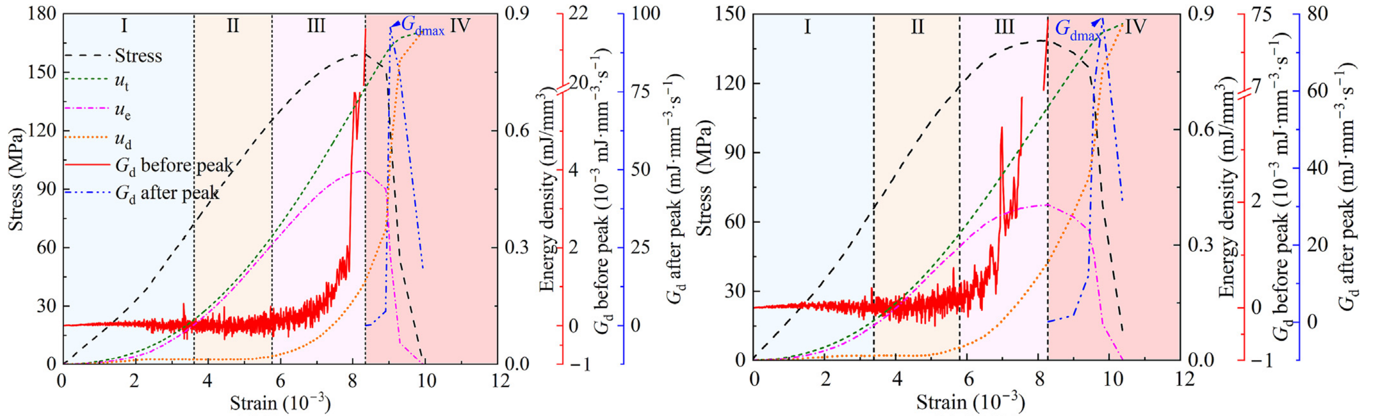

(a) Dry (b) S1/2-1

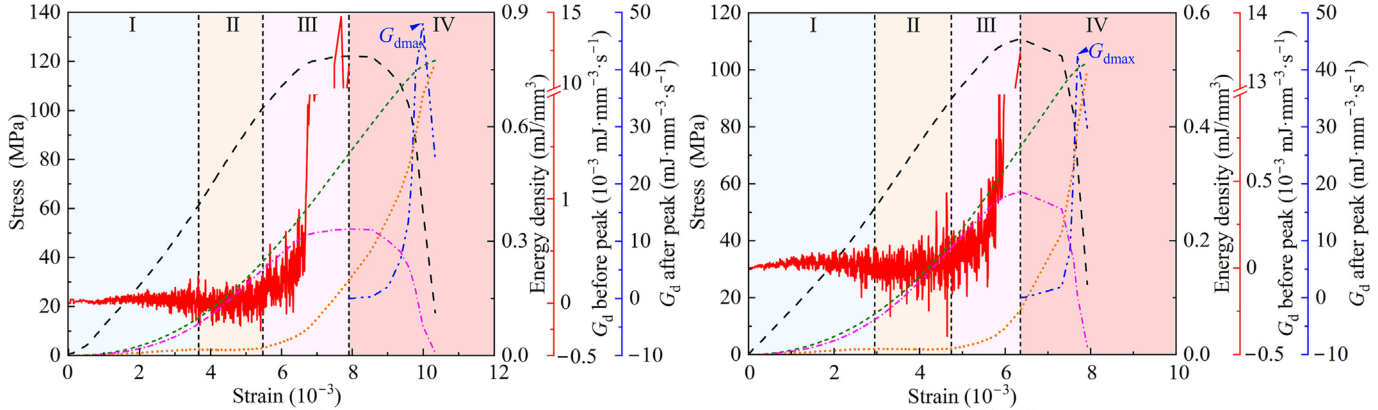

(c) S1/2-5 (d) S1/2-20

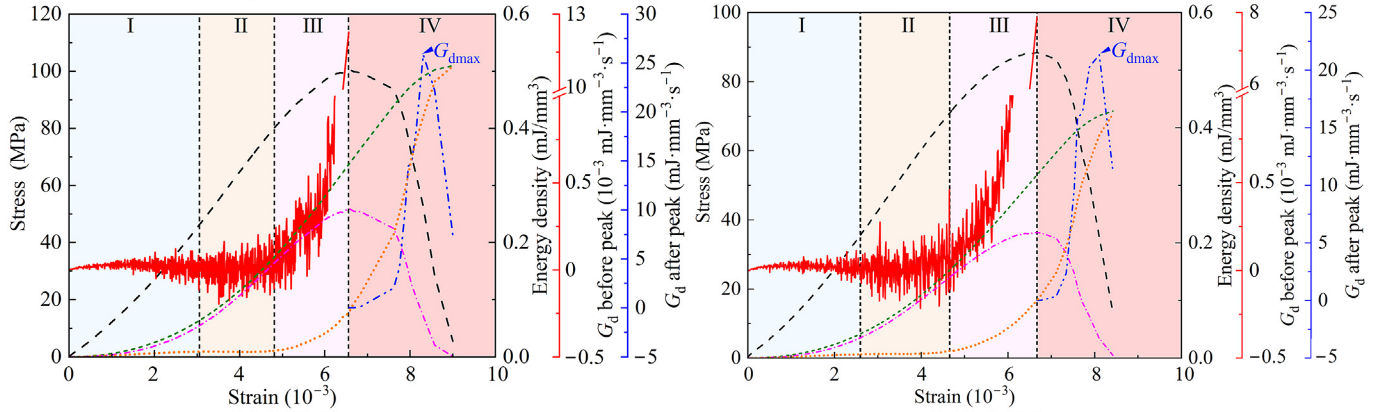

(e) S1/2-40 (f) S1/2-211

Fig. 9. Energy evolution of red sandstone specimens during UC.

is attributed to the highly limited crack propagation during this stage.

Stage III: The growth rate of u_{e} gradually slows down, while the u_{d} increases significantly and its growth rate accelerates continuously. The u_{e} curve deviates progressively from the u_{t} curve, and the G_{d} rises markedly. This is primarily due to the onset of significant crack propagation and accumulation. The accumulation of cracks leads to continuous damage to the specimen, thereby reducing the efficiency of storing elastic energy, manifesting as a continuous decline in the growth rate of u_{e}.

Stage IV: The u_{e} drops abruptly, while the u_{d} surges sharply. The G_{d} increases by thousands of times and reaches its maximum value (G_{dmax}). This is caused by the rapid release of elastic energy stored within the specimen, macroscopically manifested as the violent propagation of macroscopic cracks and the ejection of rock fragments.

Fig. 10 illustrates the evolution characteristics of the peak elastic energy density (u_{ep}) and G_{dmax} of specimens under different L with t. At various L, the u_{ep} exhibited an exponential decrease with increasing t, with a rapid decline observed within $t \leq 20$ h followed by a more gradual reduction (Fig. 10a). At t=211 h, compared with that of the dry specimen, the u_{ep} of L=1/50H, 1/8H, 1/4H, 1/2H, and H decreased by 53.4%, 56.6%, 57.8%, 58.4%, and 65.3%, respectively. Furthermore, the fitting curves indicate that, under the same t, the u_{ep} generally decreased as the L increased. In Fig. 10b, under different L, G_{dmax} decreases exponentially with increasing t, characterized by accelerated reduction within $t \leq 20$ h. At t=211 h, compared with that of the dry specimen, the G_{dmax} of L=1/50H, 1/8H, 1/4H, 1/2H, and H decreased by 69.0%, 63.8%, 75.6%, 77.6%, and 73.3%, respectively. At identical t, G_{dmax} tended to decrease with rising L. These results demonstrate that immersion not only

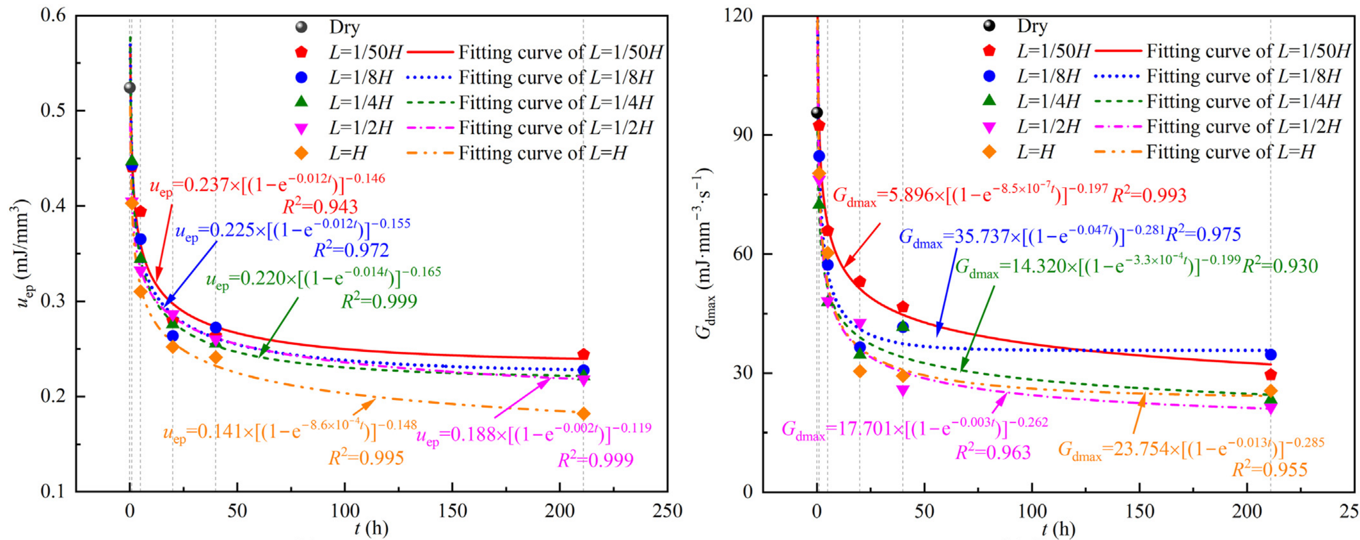

(a) u_{ep} versus t (b) G_{dmax} versus t

Fig. 10. Time-dependent energy evolution characteristics under different immersion conditions.

diminished the energy storage capacity of red sandstone but also reduced its energy dissipation capability during failure.

4.3. Failure characteristics

Figs. 11 and 12 separately illustrate the failure processes and final failure morphologies of red sandstone under various water immersion conditions. the non-uniform water distribution caused by differences in L and t significantly affected the failure characteristics of the specimens. Specimens subjected to local immersion (L≤1/2H) exhibited pronounced obvious upper and lower asymmetric failure, characterized by the following features:

(1) Temporal differences in fracture evolution: During loading, macro-cracks first emerged in the lower moistened zone. As stress increased, spalling and ejection occurred in this region, resulting in initial failure, while the upper relatively dry zone remained largely intact or only minor cracks developed.

(2) Regional differences in failure patterns: In the lower moistened zone, significant spalling occurs before specimen failure, producing thin fragments; during failure, small fragments and fine particles are ejected. In the upper relatively dry zone, the specimens maintained good integrity or developed only minor cracks prior to failure, without obvious spalling. During specimen failure, four failure patterns were observed: tensile (L≤1/4H and t≤20 h), combined tensile-shear, shear, and relatively intact conditions (L≤1/4H and t=40 h). The resulting fragments exhibited blocky and thick-flaky shapes with larger volumes.

In contrast, fully immersed specimens (L=H) and dry specimens exhibited distinctly different failure characteristics. Pre-failure cracking and spalling occurred randomly without clear temporal differences, and fragment ejection behavior was consistent between the upper and lower sections (Fig. 11). Ultimately, these specimens failed in a vertically symmetric shear (Fig. 12), with no regional difference in failure patterns. Additionally, the final failure patterns of specimens with L=1/2H closely that of fully immersed specimens, with obvious shear failure.

For locally immersed specimens (L≤1/2H), the spalling extent (including spalling depth and height) in the lower moistened zone prior to failure initially increased and subsequently decreased with prolonged t. Specifically, for specimens with L≤1/4H, the spalling extent increases in the lower moistened zone within t≤40 h, but significantly decreased at t=211 h. For specimens with L=1/2H, the spalling extent increased within t≤20 h but markedly decreased when t≥40 h. Additionally, when L≤1/4H and t=40 h, the upper relatively dry region remained intact after failure, while the lower moistened zone exhibited severe fragmentation (S1/50–40, S1/8–40, and S1/4–40 in Fig. 12). These results indicate that under specific t, the red sandstone with lower L exhibited prominent regional concentration in failure characteristics. That is, the failure mainly occurs in the lower moistened zone.

The fragmentation characteristics of rock specimens after failure partially reflect the intensity of the failure. The mean particle size (d_m) can be used to characterize the fragmentation, where a smaller d_m corresponds to smaller fragment volumes and greater quantities of debris, indicating more intense failure [30,31]. The calculation formula for the d_m is as follows:

$$d_m = \frac{\Sigma(r_i d_i)}{\Sigma r_i} \tag{4}$$

where d_i epresents the fragment size; and r_i the corresponding mass percentage of fragments with that size. For fragments smaller than 10 mm, standard sieves with apertures of 0.5, 1, 2.5, 5, and 10 mm are used for separation, and the fragment size is determined by the average aperture size of the upper and lower sieves. For fragments with sizes larger than or equal to 10 mm, their mass is measured using an electronic balance, and the fragment size is represented by the equivalent diameter.

Fig. 13 illustrates the variation of the d_m after failure for red sandstone specimens under different L over t. The results indicate that the non-uniform water distribution caused by differences in L and t significantly affects the d_m. Specifically, under full immersion conditions (L=H), d_m monotonically increases with increasing t, suggesting a gradual reduction in fragmentation. For L=1/2H, d_m exhibits a three-stage evolution: rapid increase within t≤5 h, relative stability at 5 h<t≤40 h, and significant decrease at t>40 h. For L=1/4H, d_m exhibits a unimodal trend initially increasing and then decreasing, and peaks at t=40 h. For L≤1/8H, d_m displays a characteristic of "decrease-increase–decrease", with minima at t=1h and maxima at t=40 h. Notably, d_m values for specimens with L=1/50H and t≤5 h (or L=1/8H and t≤1 h) are smaller than those under dry conditions, indicating that the degree of fragmentation in this situation is higher than that in the dry state. For specimens with L≤1/4H and t=40 h, the d_m is significantly larger than that of the L=H at t=211 h (S-211). This indicates that the degree of fragmen-

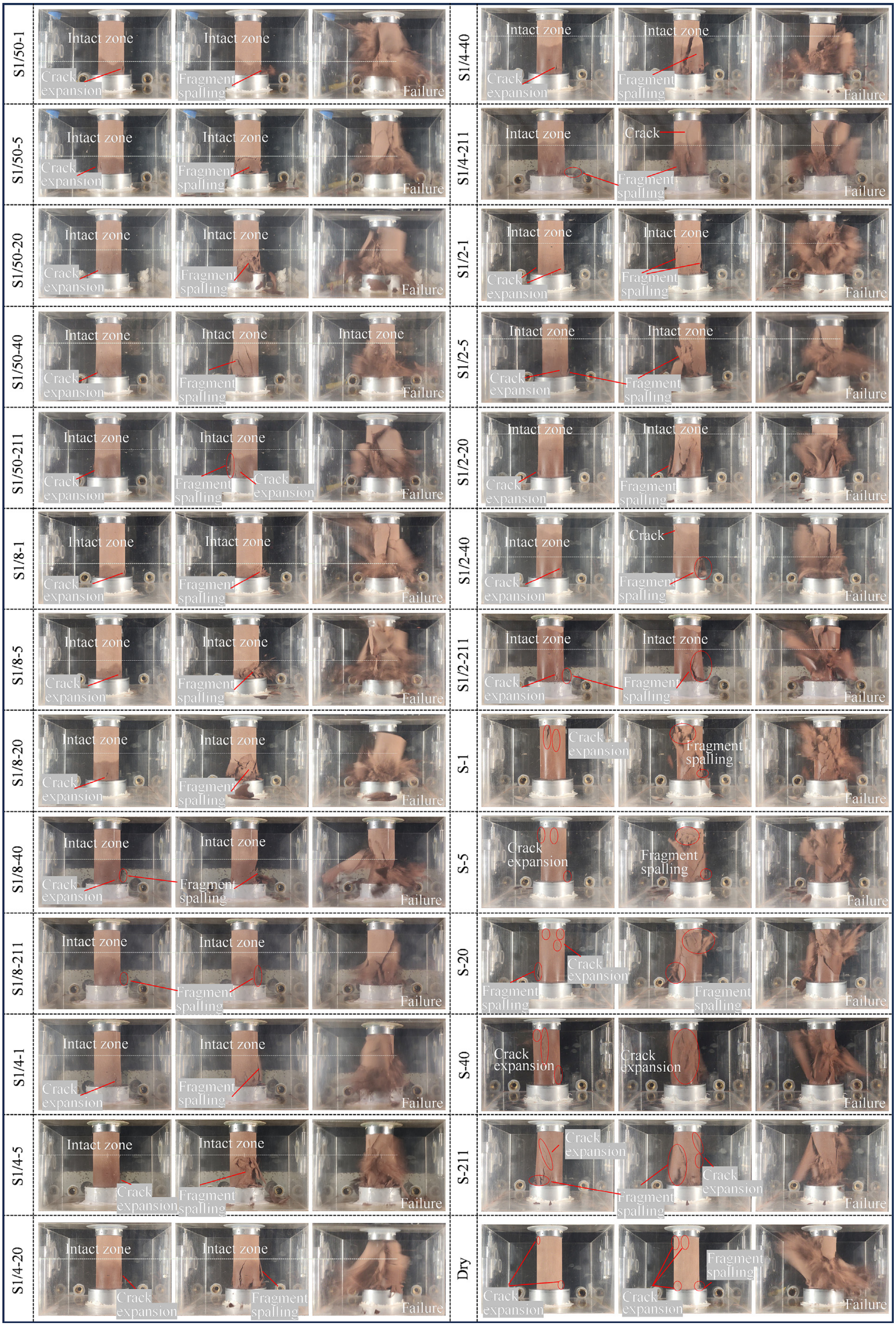

Fig. 11. Failure process of the red sandstone under different non-uniform water distribution states.

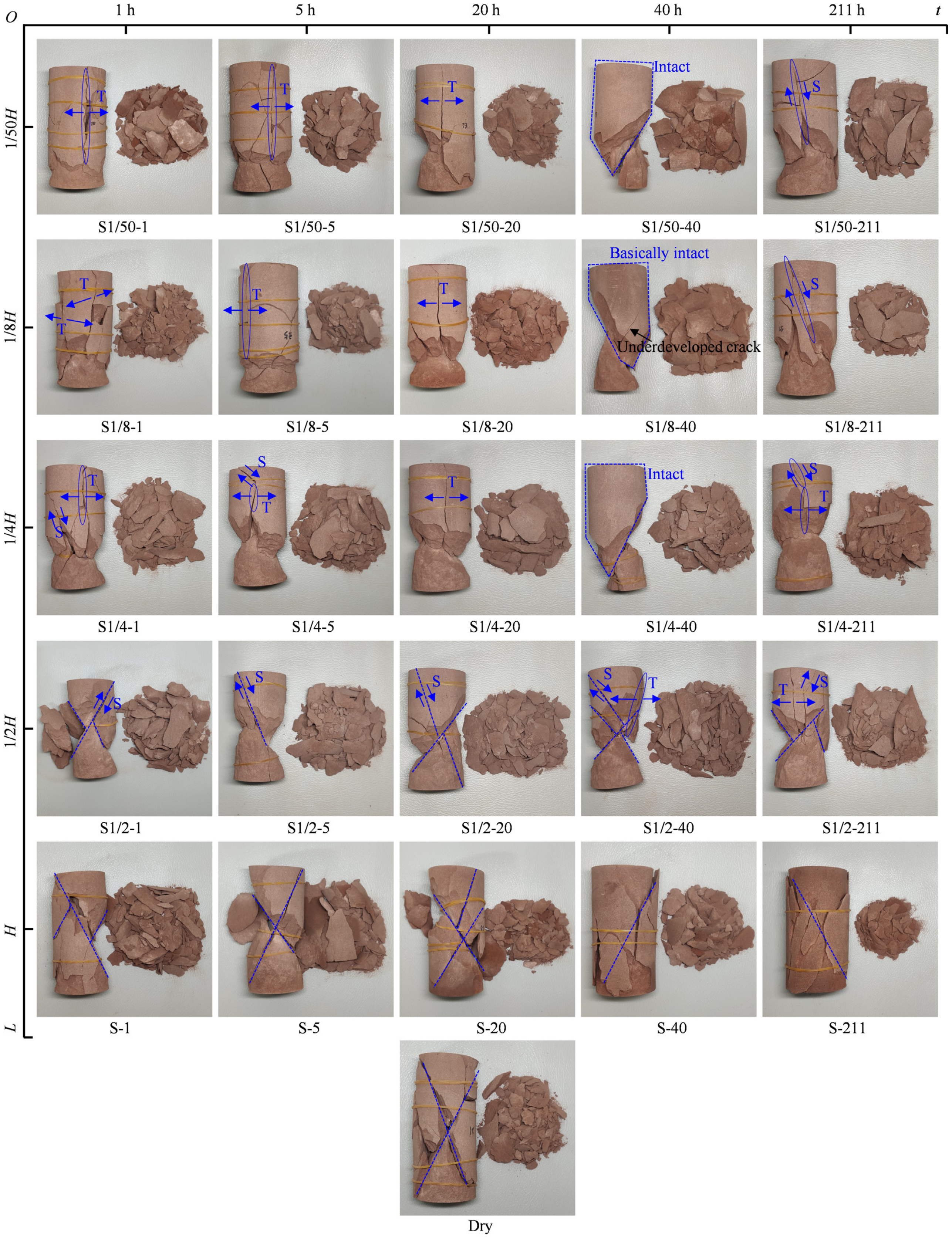

Fig. 12. Failure characteristic of the red sandstone under different non-uniform water distribution states.

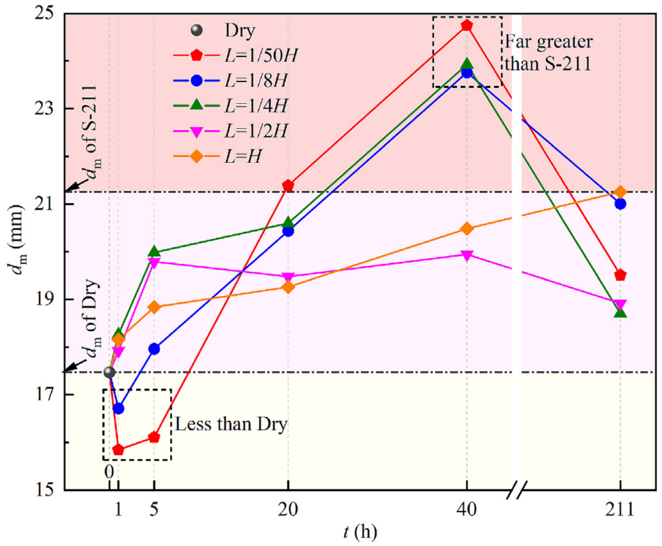

Fig. 13. Relationship between d_m and t.

tation in this situation is significantly lower than that in the fully immersed saturated state.

5. Discussion

5.1. Influence of non-uniform water distribution on the failure mechanism of red sandstone

The weakening effect of water on the mechanical properties of rock materials is a complex process involving physical and chemical interactions. The main mechanisms of this weakening include Si—O—Si hydrolysis, reduction in capillary tension, mineral dissolution, clay mineral water absorption (lubrication, softening, and expansion), and increased pore water pressure [32,33]. The increase in pore water pressure promotes microcrack propagation due to the water wedge effect, while other mechanisms primarily lead to the weakening of the rock by reducing internal friction, fracture energy, and cohesion (Fig. 14a). At the mesoscale, the weakening effect of water on rock materials manifests as a reduction in the stress threshold for microcrack initiation and propagation [14,34]. However, it is characterized by macroscopical strength degradation, E_0 decrease, deformation modulus decrease, and Poisson's ratio increase [4,30,35,36]. However, significant spatial differences in these weakening effects may exist within water-affected rocks. In this study, such spatial difference is primarily influenced by the non-uniform water distribution caused by L and t. During the immersion process of red sandstone, water gradually penetrates from the specimen surface inward, resulting an external moistened zone and an internal relatively dry zone, separated by a dry-wet interface [34,37]. In UC tests, specimens with a dry-wet interface exhibit the following characteristics in stress distribution due to the material property differences between the external moistened zone and internal dry zone (Fig. 14b): (i) The deformation modulus of rock decreases with increasing water content [35]. Therefore, the deformation modulus of the external moistened zone is lower than that of the internal dry zone, under the same axial strain, the axial stress in the external moistened zone is smaller than that in the internal dry zone (i.e., $\sigma_1<\sigma_2$). The unevenness of axial stress distribution leads to shear stress (τ) concentration at the dry-wet interface. (ii) Due to the higher Poisson's ratio of the external moistened zone, its lateral deformation exceeds that of the internal dry zone under identical axial strain, creating tensile stress (σ_{t1}) at the dry-wet interface. (iii) Ding et al. [34] found that increased pore water pressure in the moistened zone during UC generates additional tensile stress (σ_{t2}) at the dry-wet interface (indicating that additional tensile stress is generated at the dry-wet interface formed by the non-uniform water distribution in red sandstone). The cumulative effect of these three stresses ultimately leads to separation at the dry-wet interface. Therefore, the spalling accompanied by ejection observed before failure in rocks with dry-wet interfaces is closely related to this interface separation.

Based on the above analysis, we explored the failure mechanisms of red sandstone from the perspective of dry-wet interface migration and separation under different water L and t. According to the failure characteristics of red sandstone with non-uniform water distribution discussed in Section 4.3, specimens are classified into two categories. That is low L specimens ($L\leq1/4H$) and high L specimens ($L\geq1/2H$). For low L specimens, the dry-wet interface is located near the exterior during short t (Fig. 15a). Even if dry-wet interface separation occurs, the internal relatively dry zone remains capable of bearing axial stress. This explains why such specimens retain relatively high σ_c and energy storage capacity (Figs. 7 and 10a). Spalling in the moistened zone also exacerbates the uneven stress distribution within the specimen. The combination of high energy storage capacity and uneven stress distribution leads to more severe fragmentation in low L specimens compared to dry specimens (e.g., S1/50–1, S1/50–5, and S1/8–1 in Fig. 13). As t increases, the dry-wet interface gradually moves inward, reducing the size of the internal dry zone. When the dry zone shrinks to a certain extent, the separation of dry-wet interface leads to a deeper spalling depth in the lower moistened zone. After spalling, the remaining cross-sectional area in the lower part becomes very small, resulting in a sharp increase in axial stress in the lower part of the specimen. Then, the specimen fails after dry-wet interface separation due to the inability of the smaller dry zone to withstand axial stress (Fig. 15b). This results in characteristic failure where the bottom section is severely fragmented while the upper section maintains integrity (e.g., S1/50–40, S1/8–40, and S1/4–40 in Fig. 12). The inward migration of the dry-wet interface has exacerbated the spalling severity in the lower moistened zone before specimen failure. As the t further increases, the dry-wet interface separation disappears (Fig. 15c), and the spalling in lower moistened zone is not caused by the dry-wet interface separation, which explains why the spalling degree initially increases and subsequently decreases. For high L specimens, at short t, the dry-wet interface migrates inward to a shallow depth. Spalling occurs due to the separation of the dry-wet interface, and the degree of spalling increases with time (Fig. 15d). This is similar to the results observed in specimens with low L under short t. However, due to the faster W_t in specimens with high L, as time further increases, the dry-wet interface rapidly migrates inward, leading to a rapid reduction in the internal dry zone of the specimen. At this stage, the moistened zone dominates the failure of the specimen. Before reaching the stress required for dry-wet interface separation, through-cracks occur within the specimen, leading to failure (i.e., without dry-wet interface separation, Figs. 15e and f). This explains why the reduction in spalling severity in moistened zone occurs earlier in high L specimens compared to low L specimens.

Fig. 16 shows the scanning electron microscopy (SEM) results of dry-wet interface separation surfaces and other spalling fracture surfaces. The dry-wet interface separation surface (see Fig. 16a) exhibits particle pull-out pits primarily resulting from cementing layer failure. This phenomenon aligns with tensile stress characteristics and corresponds to the mechanisms of σ_{t1} and σ_{t2} shown in Fig. 14b. The overall surface is relatively smooth and flat, exhibiting layered undulating textures and debris from frictional processes, which aligns with the τ stress mechanism shown in Fig. 14b. The

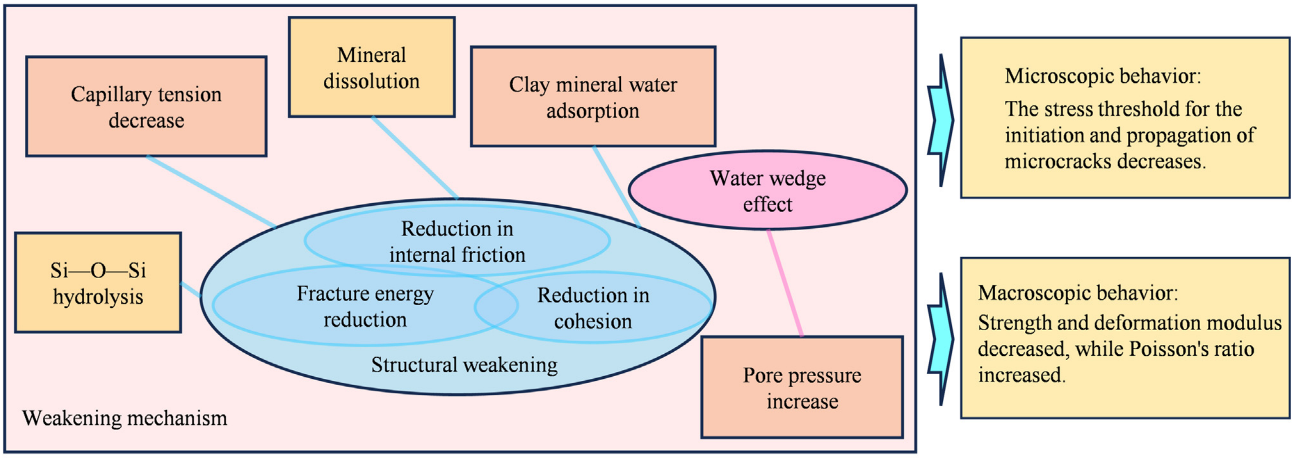

(a) Weakening mechanism of water

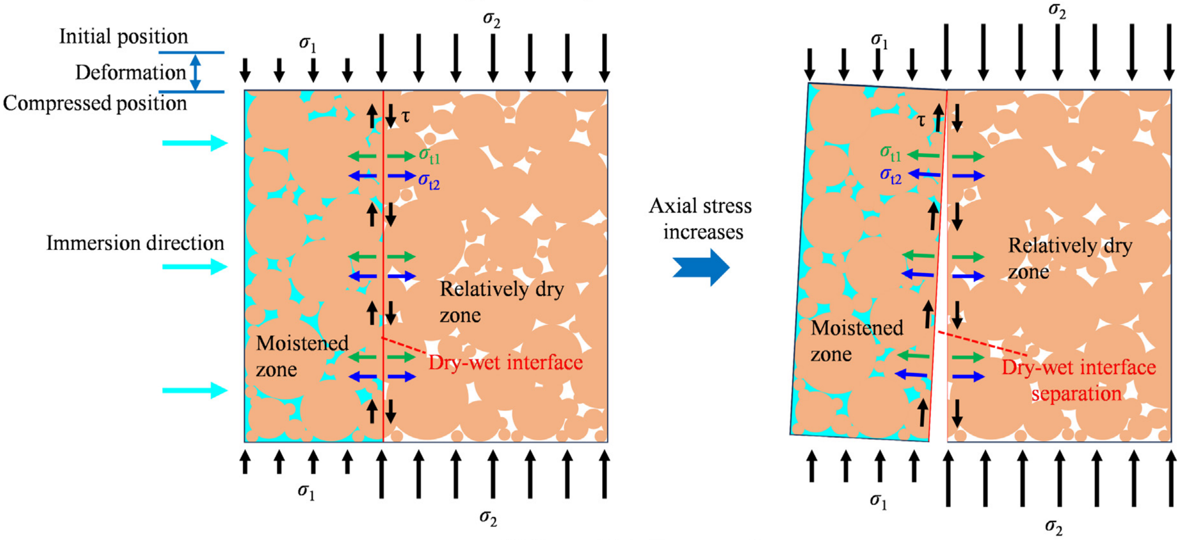

(b) Dry-wet interface separation

Fig. 14. The influence of water on red sandstone.

fracture characteristics reflect the composite stress conditions at the dry-wet interface (shear stress τ from deformation modulus differences, tensile stress σ_{t1} from lateral deformation differences, and tensile stress σ_{t2} from increased pore water pressure), exhibiting a tensile-shear mixed fracture mode. From Fig. 16b, other spalling fracture surfaces also contain particle pull-out pits, but the overall surface exhibits markedly different characteristics, showing rough and irregular surface with pronounced river patterns, tearing textures, and stepped fractures (varying texture depths and strong three-dimensional relief). Such fracture morphology conforms to typical brittle fracture characteristics induced by local stress concentration under conditions lacking macroscopic continuous weak interface guidance.

5.2. Correlations of d_m with u_{ep} and G_{dmax}

Generally, the greater the energy release amount and release rate, the more intense the failure and the higher the fragmentation degree [24,38,39]. The u_{ep} and G_{dmax} can reflect the energy release amount and release rate during rock failure to some extent. Hence, these two indicators can be used to evaluate the intensity of rock failure [12,28,29]. To evaluate the applicability of these two indicators under different water immersion conditions, the correlation between d_{m} and these two indicators was analyzed. As shown in Figs. 17a and b, under full immersion conditions (L=H), d_{m} showed a good linear negative correlation with both u_{ep} and G_{dmax}, with the fitting correlation coefficients reaching 0.860 and 0.835, respectively. It indicates that these two indicators can effectively characterize the failure intensity of fully immersed rocks to some extent. However, under local immersion conditions ($L\leq1/2H$), d_{m} exhibited obvious irregularity and low correlation with these two indicators. This indicates that the applicability of traditional energy indicators is limited under local immersion (i.e., non-uniform water distribution) conditions. Especially under low L and short-term immersion conditions (L=1/50H and $t\leq5$ h, L=1/8H and $t\leq1$h), although energy indicators decrease compared to those under dry conditions, the actual fragmentation degree is higher than that under dry conditions. Based on the analysis in Section 5.1, it can be concluded that this phenomenon can be attributed to the following three reasons caused by the non-uniform water distribution: (1) The moistened zone is prone to spalling, resulting in a reduction of the load-bearing cross-sectional area. This reduction significantly increases stress, and since higher stress corresponds to greater stored energy, the failure becomes more severe. (2) The difference in water content on both sides of the dry-wet interface leads to a discrepancy in rock stiffness, which in turn causes stress concentration at the dry-wet interface. The concentrated stress promotes the initiation and propagation of more cracks. (3) The moistened

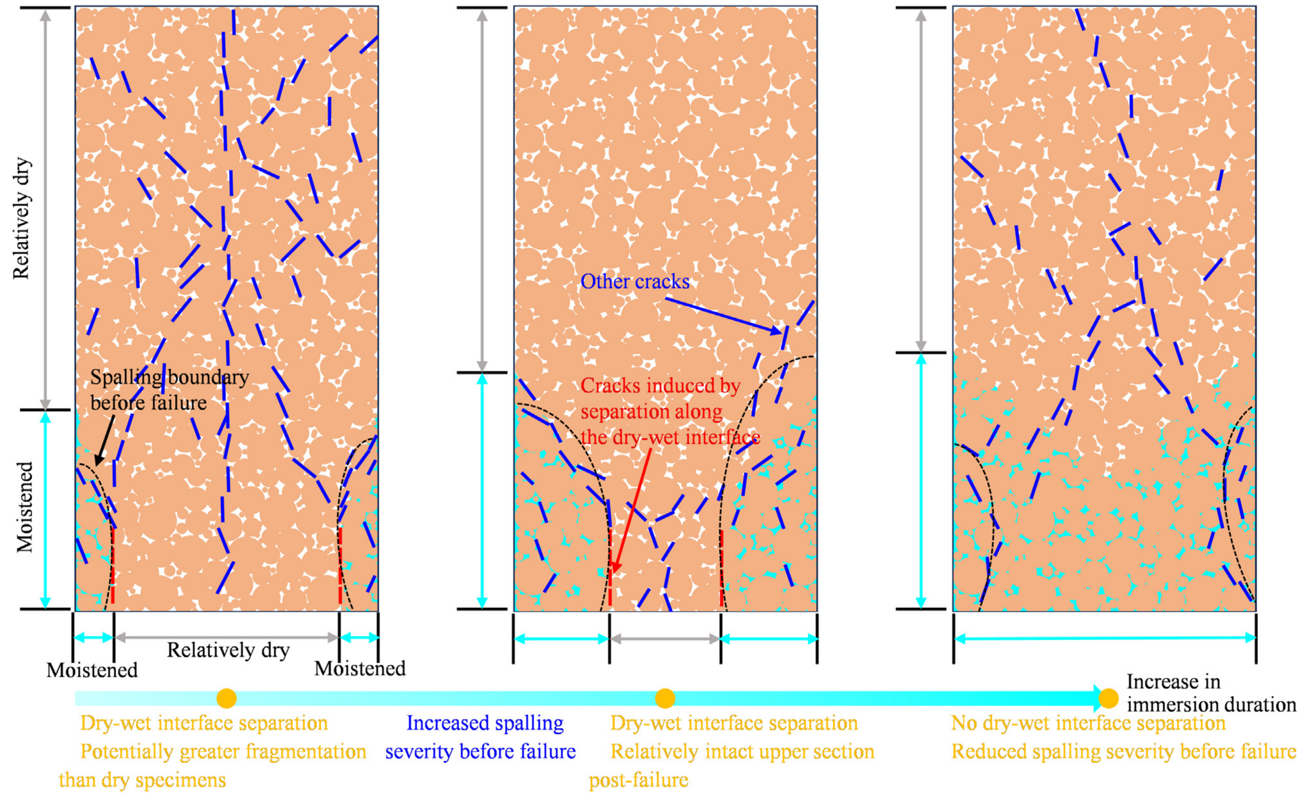

(a) Short *t* at low *L* (b) Longer *t* at low *L* (c) Long *t* at low *L*

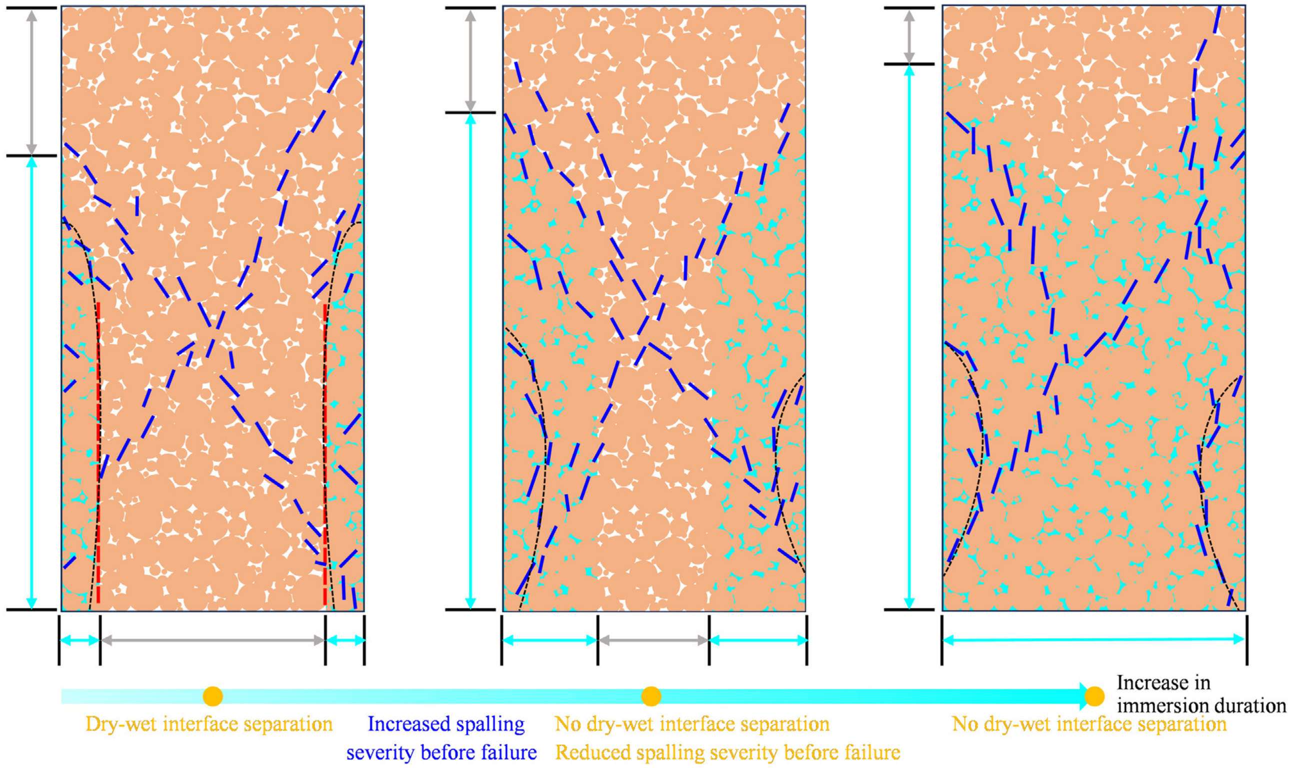

(d) Short *t* at high *L* (e) Longer *t* at high *L* (f) Long *t* at high *L*

Fig. 15. Schematic diagram of spalling evolution under different immersion conditions.

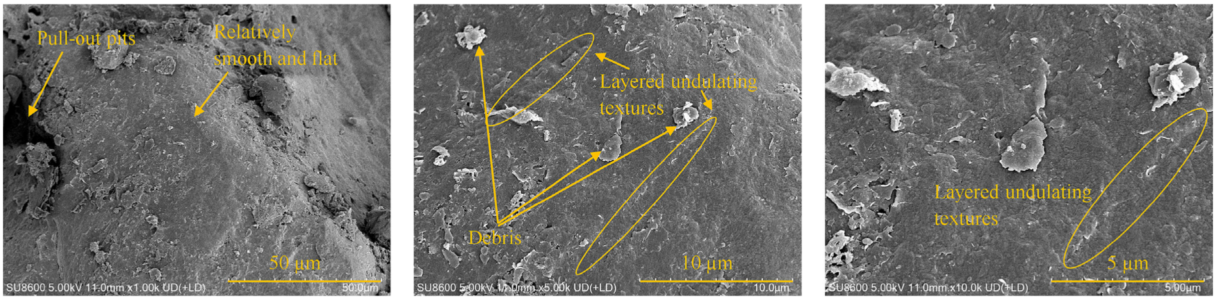

(a) Dry-wet interface separation surfaces

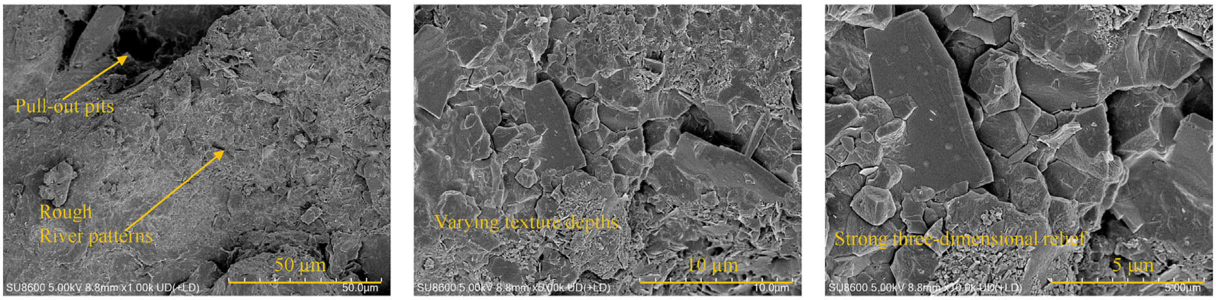

(b) Other spalling fracture surfaces

Fig. 16. SEM images of dry-wet interface separation surfaces and other spalling fracture surfaces.

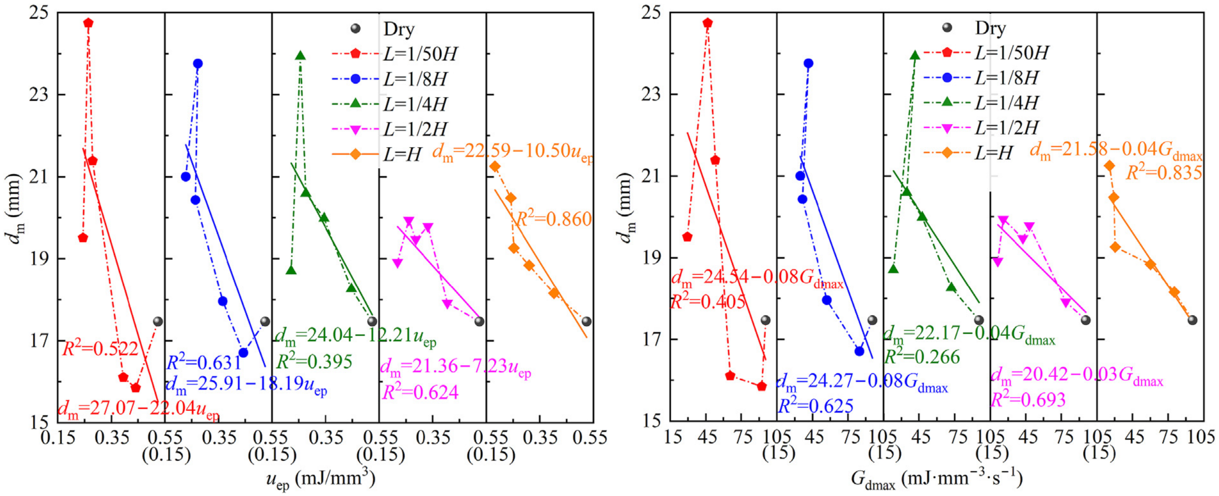

(a) Relationship between d_m and u_{ep} (b) Relationship between d_m and G_{dmax}

Fig. 17. Correlations of d_m with u_{ep} and G_{dmax}.

zone has a high-water content, where capillary forces exist. These capillary forces facilitate the propagation of cracks.

5.3. Influence of non-uniform water distribution on the strength of red sandstone

The σ_c of fully immersed sandstone specimens exponentially decreases with increasing W_t [4]. As shown in Fig. 18a, under different L, the σ_c decreases exponentially with increasing W_t, and at identical W_t, the σ_c generally reduces as the L decreases. To reveal the relationship between σ_c and L in red sandstone under the same W_t, a series of UC tests were added under the same W_t. The experimental scheme is detailed in Table 2, involving three water absorption levels (i.e., W_{t8}, 0.5W_{t8}, 0.2W_{t8}, where W_{t8} represents the natural W_t of red sandstone with L=1/8H) and four L (i.e., H, 1/2H, 1/4H, and 1/8H). Specimen preparation, loading method, and loading rate remained consistent with Section 2.2. The measured σ_c and actual W_t are presented in Fig. 18b. At the same W_t, the σ_c nonlinearly decreases with reducing L, and the rate of reduction accelerates progressively. Specifically, when the L decreases from H to 1/8H, the σ_c at W_{t8}, 0.5W_{t8}, and 0.2W_{t8} decline by 10.2%, 9.3%, and 15.4%, respectively, with the σ_c decrease mainly occurring at $L \leq 1/2H$. This indicates that even under identical W_t, distinct non-uniform water distributions significantly affect red sandstone strength, with L being a critical factor, particularly when $L \leq 1/2H$. Existing studies have shown that the mechanical properties degradation of rock materials positively correlates with their water content [40]. Under the same W_t, reducing L leads to a more localized water concentration, elevated water content in moistened zones, greater weakening effects, and lower stress thresholds for fracture (Fig. 19). Since UC applies equal axial stress across the specimen, localized fracture in low L specimens initiates at lower stress. Such localized fracture further accelerates the overall failure, thereby causing specimens with lower L to fail at a lower stress under the same W_t. Therefore, when evaluating the weakening effect of water on the strength of rocks, the concentration

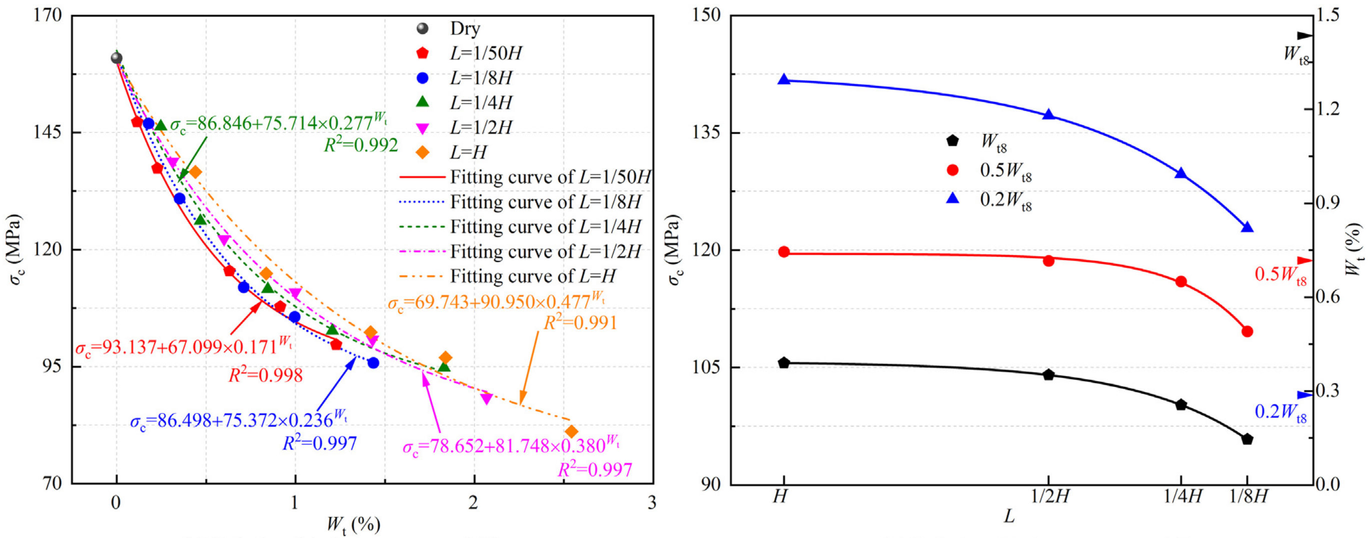

(a) Relationship between σ_c and W_t

(b) Relationship between σ_c and L

Fig. 18. Correlations of σ_c with W_t and L.

Table 2
UC scheme of red sandstone with the same W_t.

W_t	W_{t8}				$0.5W_{t8}$				$0.2W_{t8}$			
L	H	1/2H	1/4H	1/8H	H	1/2H	1/4H	1/8H	H	1/2H	1/4H	1/8H

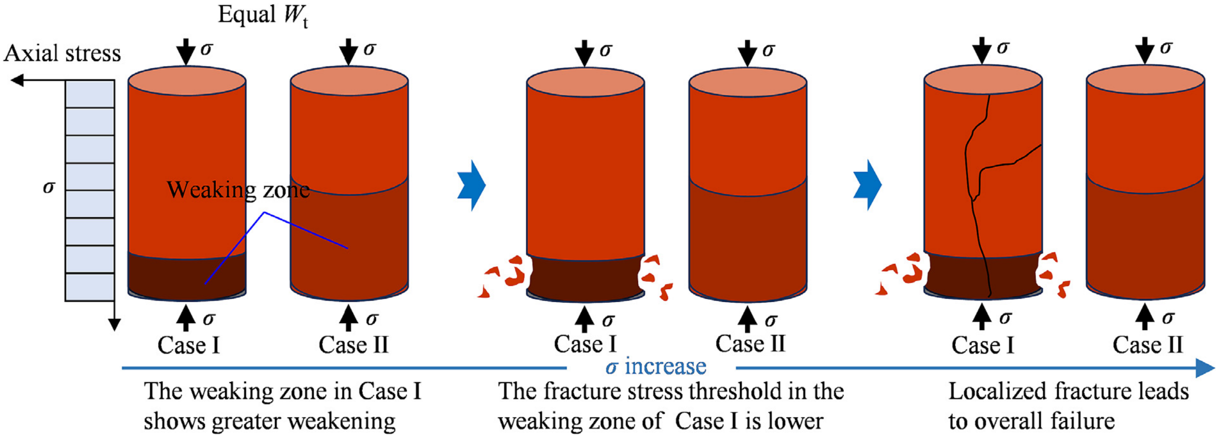

Fig. 19. Fracture patterns under different L at constant W_t.

degree of non-uniform water distribution (C=W_t×(total volume/moistened zone volume)) is a critical factor.

5.4. Harmful effects of low immersion height on underground rock engineering

The construction process of underground rock engineering and groundwater activity may lead to water accumulation, subjecting rock structures to low L [1]. The non-uniform water distribution caused by low L significantly affects the stability of underground rock structures. Taking L=1/50H as an example, the hazards of non-uniform water distribution caused by low L are analyzed from two aspects: strength weakening and failure intensity. In Fig. 20a, the strength weakening levels of the L=1/50H specimens relative to the dry sspecimens at 1, 5, 20, 40, and 211 h reached 8.5%, 14.7%, 28.3%, 33.0%, and 38.0%, respectively. The relative strength weakening of L=H specimens at 1, 5, 20, 40, and 211 h were 15.1%, 28.6%, 36.4%, 39.8%, and 49.6%, respectively. Further analysis shows that the strength weakening of L=1/50H specimens at 1, 5, 20, 40, and 211 h reach 56.3%, 51.4%, 77.7%, 82.9%, and 76.6% of those under L=H conditions, respectively. These results indicate that under low L, the strength weakening increase with t and stabilize after t≥20 h, reaching over 75% of the weakening under full immersion conditions. In Fig. 20b, the d_m of L=1/50H specimens decreases by 9.3% and 7.8% relative to dry specimens at t=1 and 5 h, respectively, but increases by 22.4%, 41.6%, and 9.1% at t=20, 40, and 211 h, respectively. In contrast, the d_m of L=H specimens consistently increases, showing relative increases of 3.9%, 7.8%,

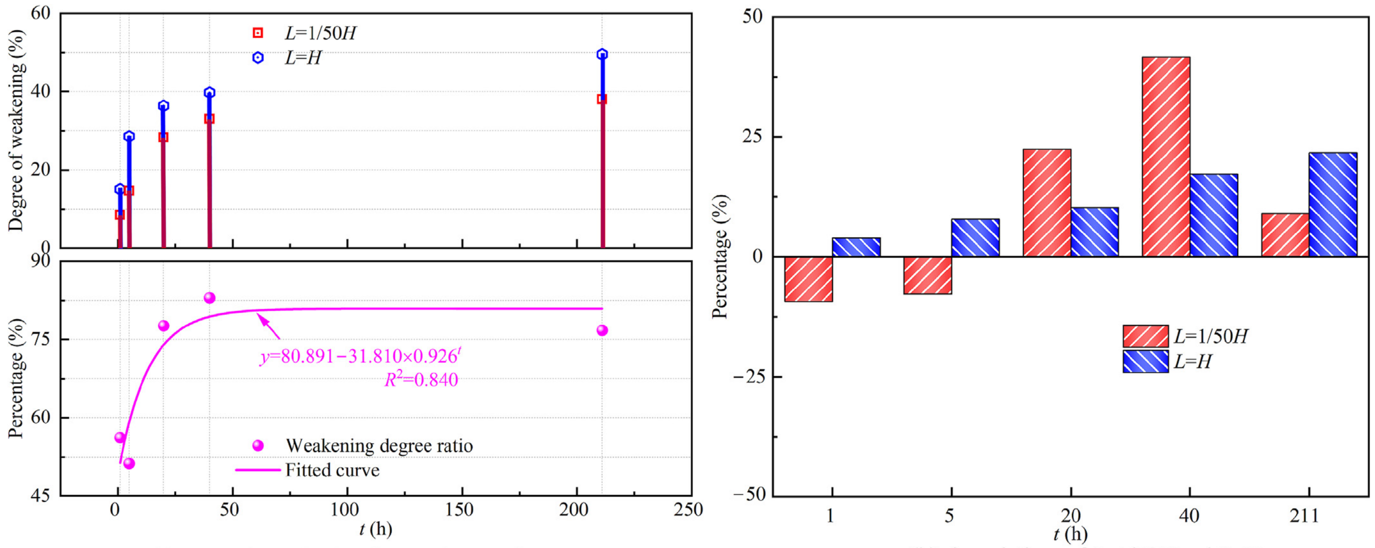

(a) Strength weakening for L=1/50H and L=H

(b) d_m variations of L=1/50H and L=H

Fig. 20. Evolution of strength weakening and d_m variation with t relative to dry specimens.

10.3%, 17.3%, and 21.7% compared to dry specimens at t=1, 5, 20, 40, and 211 h, respectively. The d_m of L=1/50H specimens is smaller than that of L=H at t=1, 5, and 211 h but greater at t=20 and 40 h.

Based on the above analysis, the hazards of non-uniform water distribution under low L on red sandstone underground structures can be divided into three periods:

(1) Short-term immersion (t≤5 h): The strength weakening reaches 14.7% (exceeding 50% of the strength weakening under corresponding full immersion conditions), and the fragmentation degree exceeds that under full immersion or even dry conditions.

(22) Mid-term immersion (5 h<t≤40 h): The strength weakening reaches 33.0% (exceeding 75% of the strength weakening under corresponding full immersion conditions), with a fragmentation degree lower than that under full immersion.

(3) Long-term immersion (t>40 h): The weakening reaches 38.0% (exceeding 75% of the strength weakening under corresponding full immersion conditions), and the fragmentation degree exceeds that under full immersion.

Therefore, in underground rock structures with low L, short-term immersion leading to non-uniform water distribution primarily causes significant weakening of surrounding rock strength, but results in intense rock failure. In contrast, medium-to-long-term immersion causing non-uniform water distribution mainly leads to severe strength weakening of the surrounding rock. For underground surrounding rocks that may be affected by local immersion, the drainage system at the bottom of the surrounding rock should be improved (such as setting up drainage ditches, collection wells, etc.). Meanwhile, waterproof treatment should be carried out on the bottom of the important bearing surrounding rock (such as spraying waterproof materials, setting waterproof curtains, etc.) to avoid non-uniform water distribution in the surrounding rock at low L and ensure the long-term stability of underground rock engineering.

It is noteworthy that current research is solely based on laboratory experiments, which have certain limitations. There are certain differences between actual rock masses and laboratory specimens, such as scale, heterogeneity, and complex boundary conditions. Additionally, the actual groundwater may contain various chemical components and exhibit different pH values, which vary from region to region. These factors are likely to influence the experimental results. This study primarily focuses on the effects of water on the mechanical properties and failure behaviors of red sandstone, revealing the weakening mechanisms of non-uniform water distribution on red sandstone from a macroscopic perspective. The findings can provide theoretical references for future research on the effects of non-uniform water distribution on surrounding rocks under complex water environments that align with engineering practices.

6. Conclusions

(1) The W_t and water distribution of red sandstone are controlled by the immersion height and duration, even under L<1/50H, the W_t can reach approximately half of that of full immersion under long-term immersion.

(2) The peak strength, elastic modulus and failure intensity of red sandstone are sensitive to immersion height, exhibiting significant weakening effects even under L<1/50H. Red sandstone with L≤1/2H exhibits distinct upper and lower asymmetric failure, characterized by temporal in fracture evolution and regional in failure patterns. For red sandstone with L>1/2H or dry state, the initial fracturing and spalling locations appear randomly, exhibiting upper and lower symmetric failure. The C is the critical factor in evaluating the weakening effect of immersion on rock strength.

(3) Immersion effect not only reduces the energy storage limit of red sandstone but also diminishes its energy dissipation capacity during failure. Under full-immersion conditions, the u_{ep} and G_{dmax} demonstrate strong linear negative correlations with the d_m. Under local immersion conditions, the traditional energy indicators have limitations in assessing the intensity of rock failure.

(4) The dry-wet interface migration and separation caused by different immersion heights and durations control the failure mode of red sandstone. Under L≤1/4H, at t≤20 h, the dry-wet interface separation leads to spalling in the outer side of the interface, and the upper dry zone exhibits tensile failure. At t=40 h, the dry-wet interface separation causes severe failure on both sides of the interface, no failure occurs in the upper dry zone. At t≥211 h, the dry-wet interface separation disappears, the upper dry zone exhibits shear failure. Under L≥1/2H, the time required for disappearance is shortened, exhibiting vertically symmetric shear failure.

Acknowledgements

This work has been supported by the National Natural Science Foundation of China (Nos. 52474133, 52304227, 52304091, and 52374095), and the Natural Science Foundation of Hunan Province (Nos. 2025JJ50316 and 2023JJ40548).

References

[1] Chen PZ, Tang SB, Liang X, Zhang YJ, Tang CN. The influence of immersed water level on the short- and long-term mechanical behavior of sandstone. Int J Rock Mech Min Sci 2021;138:104631.

[2] Luo Y, Huang JC, Wu WX, Si XF, Zhu CQ. Saturation effect on storage-dissipation properties and failure characteristics of red sandstone: Energy mechanism of water in preventing rockburst. Int J Coal Sci Technol 2025;12(1):32.

[3] Price NJ. The compressive strength of coal measure rocks. Colliery Eng 1960;37(437):283–92.

[4] Hawkins AB, McConnell BJ. Sensitivity of sandstone strength and deformability to changes in moisture content. Q J Eng Geol 1992;25(2):115–30.

[5] Simpson DR, Fergus Jr JH. The effect of water on the compressive strength of diabase. J Geophys Res 1968;73(20):6591–4.

[6] Zhu J, Deng JH, Chen F, Huang YM, Yu ZQ. Water saturation effects on mechanical and fracture behavior of marble. Int J Geomech 2020;20(10):04020191.

[7] Yilmaz I. Influence of water content on the strength and deformability of gypsum. Int J Rock Mech Min Sci 2010;47(2):342–7.

[8] Wong LNY, Maruvanchery V, Liu G. Water effects on rock strength and stiffness degradation. Acta Geotech 2016;11(4):713–37.

[9] Niu SJ, Ge SS, Yang DF, Dang YH, Yu J, Zhang S. Mechanical properties and energy mechanism of saturated sandstones. J Cent South Univ 2018;25(6):1447–63.

[10] Khan NM, Ma LQ, Cao KW, Hussain S, Liu W, Xu YJ, Yuan QP, Gu J. Prediction of an early failure point using infrared radiation characteristics and energy evolution for sandstone with different water contents. Bull Eng Geol Environ 2021;80(9):6913–36.

[11] Zhou ZL, Wang PY, Cai X, Cao WZ. Influence of water content on energy partition and release in rock failure: Implications for water-weakening on rock-burst proneness. Rock Mech Rock Eng 2023;56(9):6189–205.

[12] Luo S, Gong FQ, Peng K, Liu ZX. Influence of water on rockburst proneness of sandstone: Insights from relative and absolute energy storage. Eng Geol 2023;323:107172.

[13] Li CM, Liu N, Liu WR, Feng RM. Study on characteristics of energy storage and acoustic emission of rock under different moisture content. Sustainability 2021;13(3):1041.

[14] Zhou ZL, Cai X, Ma D, Cao WZ, Chen L, Zhou J. Effects of water content on fracture and mechanical behavior of sandstone with a low clay mineral content. Eng Fract Mech 2018;193:47–65.

[15] Cai X, Zhou ZL, Zang HZ, Song ZY. Water saturation effects on dynamic behavior and microstructure damage of sandstone: Phenomena and mechanisms. Eng Geol 2020;276:105760.

[16] Cai X, Zhou ZL, Liu KW, Du XM, Zang HZ. Water-weakening effects on the mechanical behavior of different rock types: Phenomena and mechanisms. Appl Sci 2019;9(20):4450.

[17] Liu G, Wang SX, Wang DW, Yang ZT, Zan YL. Characteristics of deformation and damage and acoustic properties of sandstone in circular tunnel morphology under varying inundation depths. Water 2024;16(20):2938.

[18] Yu LQ, Yao QL, Liu JF, Li XH, Chong ZH, Wang FR, Xie HX, Li YH. Effect of spatial distribution of water on rock mechanical properties and characterization of water diffusion. Constr Build Mater 2025;470:140551.

[19] Luo Y, Li SP, Huang JC, Chen BW, Dong JL. Deformation and failure characteristics of uniaxial compression prestressed red sandstone under short-term immersion conditions. Int J Energy Res 2025;2025(1):9202005.

[20] Liu HD, Liu S, Liu HN, Chen JX, Xia ZG, Zhai JY, Fu YY. Mechanical deterioration effect and damage evolution characteristics of soft sandstone with different water immersed heights under uniaxial compression. Bull Eng Geol Environ 2023;82(4):154.

[21] Si XF, Luo Y, Gong FQ, Huang JC, Han KF. Temperature effect of rockburst in granite Caverns: Insights from reduced-scale model true-triaxial test. Geomech Geophys Geo Energy Geo Resour 2024;10(1):26.

[22] Wang XF, Jiang T, Zhu CQ, Wei YY, Jiang YH. Mechanical manifestation characteristics and damage evolution law of unloading perturbation damage in surrounding rock of deep roadways. Geomech Geophys Geo Energy Geo Resour 2025;11(1):35.

[23] Tan YL, Tan Y, Guo WY, Li B, He SD, Zhang L, Zhang YJ, Zhang QY. Calculation model for kinetic energy and rock burst risk evaluation method during roadway excavation. Int J Min Sci Technol 2025;35(5):677–90.

[24] Wang JA, Park HD. Comprehensive prediction of rockburst based on analysis of strain energy in rocks. Tunn Undergr Space Technol 2001;16(1):49–57.

[25] Xie HP, Li LY, Peng RD, Ju Y. Energy analysis and criteria for structural failure of rocks. J Rock Mech Geotech Eng 2009;1(1):11–20.

[26] Heap MJ, Faulkner DR, Meredith PG, Vinciguerra S. Elastic moduli evolution and accompanying stress changes with increasing crack damage: Implications for stress changes around fault zones and volcanoes during deformation. Geophys J Int 2010;183(1):225–36.

[27] Li P, Cai MF. Energy evolution mechanism and failure criteria of jointed surrounding rock under uniaxial compression. J Cent South Univ 2021;28(6):1857–74.

[28] Zhang RJ, Liu YR, Hou SK. Evaluation of rockburst risk in deep tunnels considering structural planes based on energy dissipation rate criterion and numerical simulation. Tunn Undergr Space Technol 2023;137:105128.

[29] Liu YR, Zhang RJ, Hou SK, Zhu L, Pang ZY, Zhuang WY. Investigation of energy evolution process of rock mass during deep tunnel excavation based on elasto-viscoplastic damage model and time-dependent energy indices. Acta Geotech 2025;20(4):1549–70.

[30] Luo Y, Huang JC, Si XF, Wu WX, Li SP. Failure characteristics and energy properties of red sandstone under uniaxial compression: Water content effect and its application. Bull Eng Geol Environ 2025;84(1):57.

[31] Si XF, Zhang ZL, Li XB, Yi GS, Luo Y, Tan LH. Influences of maximum principal stress direction and cross-section shape on tunnel stability. J Rock Mech Geotech Eng 2025;17(4):2159–80.

[32] Wasantha PLP, Ranjith PG, Permata G, Bing D. Damage evolution and deformation behaviour of dry and saturated sandstones: Insights gleaned from optical measurements. Measurement 2018;130:8–17.

[33] Cadoni E, Labibes K, Albertini C, Berra M, Giangrasso M. Strain-rate effect on the tensile behaviour of concrete at different relative humidity levels. Mater Struct 2001;34(1):21–6.

[34] Ding S, Tang SB, Jia HL, Li YB. The influence of water on the failure characteristics of sandstone under uniaxial compression conditions by acoustic emission and NMR observation. Eng Geol 2023;322:107173.

[35] Zhang W, Zhang DX, Guo WY, Zhang BL. Experimental study on failure precursory characteristics and moisture content effect of pre-cracked rocks under graded cyclic loading and unloading. Int J Min Sci Technol 2025;35(2):249–64.

[36] Zhu C, Xu XD, Liu WR, Xiong F, Lin Y, Cao C, Liu X. Softening damage analysis of gypsum rock with water immersion time based on laboratory experiment. IEEE Access 2019;7:125575–85.

[37] Zhou ZL, Cai X, Cao WZ, Li XB, Xiong C. Influence of water content on mechanical properties of rock in both saturation and drying processes. Rock Mech Rock Eng 2016;49(8):3009–25.

[38] Luo Y, Huang JC, Si XF, Lin F, Wu WX. An energy-based method for uniaxially compressed rocks and its implication. J Rock Mech Geotech Eng 2025;17(3):1429–44.

[39] Peng K, Liu X, Huang WS, He HY, Ren J, Luo S. The role of minimum principal stress in tunnel strainburst considering spatial structure effect. Theor Appl Fract Mech 2025;139:105085.

[40] Han PH, Zhang C, Wang XJ, Wang L. Study of mechanical characteristics and damage mechanism of sandstone under long-term immersion. Eng Geol 2023;315:107020.